Article

H-ATLAS: the far-infrared properties of galaxies in and around the coma cluster

Fuller, C, Davies, JI, Smith, MWL, Valiante, E, Eales, S, Bourne, N, Dunne, L, Dye, S, Furlanetto, C, Ibar, E, Ivison, R, Maddox, S, Sansom, AE, Michałowski, MJ and Davis, T

Fuller, C, Davies, JI, Smith, MWL, Valiante, E, Eales, S, Bourne, N, Dunne, L, Dye, S, Furlanetto, C, Ibar, E, Ivison, R, Maddox, S, Sansom, AE, Michałowski, MJ and Davis, T (2016) H-ATLAS: the far-infrared properties of galaxies in and around the coma cluster. Monthly Notices of the Royal Astronomical Society, 458 (1). pp. 582-602. ISSN 0035-8711

Monthly Notices
of the
ROYAL ASTRONOMICAL SOCIETY

MNRAS **458,** 582–602 (2016)
Advance Access publication 2016 February 10

doi:10.1093/mnras/stw305

H-ATLAS: the far-infrared properties of galaxies in and around the Coma cluster

C. Fuller,[1] J. I. Davies,[1⋆] M. W. L. Smith,[1] E. Valiante,[1] S. Eales,[1] N. Bourne,[2] L. Dunne,[1,2] S. Dye,[3] C. Furlanetto,[4] E. Ibar,[4] R. Ivison,[2,5] S. Maddox,[1,2] A. Sansom,[6] M. J. Michałowski[2] and T. Davis[1]

[1]*School of Physics and Astronomy, Cardiff University, The Parade, Cardiff CF24 3AA, UK*
[2]*Institute for Astronomy, University of Edinburgh, Royal Observatory, Blackford Hill, Edinburgh EH9 3HJ, UK*
[3]*School of Physics and Astronomy, University of Nottingham, University Park, Nottingham NG7 2RD, UK*
[4]*Instituto de Física y Astronomía, Universidad de Valparaíso, Avda. Gran Bretaña 1111, Valparaíso, Chile*
[5]*European Southern Observatory, Karl-Schwarzschild-Strasse 2, D-85748 Garching, Germany*
[6]*SUPA, Institute for Astronomy, University of Edinburgh, Royal Observatory, Edinburgh EH9 3HJ, UK*

Accepted 2016 February 5. Received 2016 February 5; in original form 2015 October 6

ABSTRACT

We describe a far-infrared survey of the Coma cluster and the galaxy filament it resides within. Our survey covers an area of ∼150 deg^2 observed by *Herschel* H-ATLAS (*Herschel* Astrophysical Terahertz Large Area Survey) in five bands at 100, 160, 250, 350 and 500 μm. The SDSS spectroscopic survey ($m_r \leq 17.8$) is used to define an area (within the virial radius) and redshift selected ($4268 < v < 9700$ km s^{-1}) sample of 744 Coma cluster galaxies – the Coma Cluster Catalogue. For comparison, we also define a sample of 951 galaxies in the connecting filament – the Coma Filament Catalogue. The optical positions and parameters are used to define appropriate apertures to measure each galaxy's far-infrared emission. We have detected 99 of 744 (13 per cent) and 422 of 951 (44 per cent) of the cluster and filament galaxies in the SPIRE 250 μm band. We consider the relative detection rates of galaxies of different morphological types finding that it is only the S0/Sa population that shows clear differences between the cluster and filament. We find no differences between the dust masses and temperatures of cluster and filament galaxies with the exception of early-type galaxy dust temperatures, which are significantly hotter in the cluster than in the filament (X-ray heating?). From a chemical evolution model, we find no evidence for different evolutionary processes (gas loss or infall) between galaxies in the cluster and filament.

Key words: galaxies: clusters: individual: Coma – galaxies: ISM – galaxies: photometry – infrared: galaxies.

1 INTRODUCTION

The Coma cluster is a local example of a giant relaxed structure. Coma is located at a distance of ∼100 Mpc, has a mass of $\sim 10^{15}$ M$_\odot$ and a virial radius ∼3 Mpc (Girardi et al. 1998; Boselli & Gavazzi 2006). The cluster resides in a large filamentary structure known as the 'Great Wall', which is an overdensity (galactic filament) of galaxies linking Coma with other groups and clusters including another nearby cluster A1367 (Ramella, Geller & Huchra 1992). The cluster resides at a high galactic latitude of $b = 88.^\circ0$, making it ideal for extragalactic studies at all wavelengths. Notably observed using the 48 inch reflector on Mount Wilson by Zwicky (1951), it was not until 1983 that Godwin & Peach (1977) created the most cited optical catalogue of 'Coma' galaxies. They catalogued over 6000 galaxies in the region of the cluster, but not all of these are cluster members as the origin of their data was photographic plate imaging, with no spectroscopy to distinguish cluster members from the foreground/background. For this reason, an important first part of our project has been to produce an optical catalogue of Coma cluster members that can be used in the same way as that used for other nearby clusters such as Virgo (Virgo Cluster Catalogue, VCC; Binggeli, Sandage & Tammann 1985) and Fornax (Fornax Cluster Catalogue, FCC; Ferguson 1989).

Compared to a cluster like Virgo, Coma has a much more centrally concentrated distribution of galaxies and mass. The latter can be inferred from the X-ray emitting gas (Colless & Dunn 1995), which is thought to be material originally lost by member galaxies,

⋆E-mail: Jonathan.Davies@astro.cf.ac.uk

that now traces the gravitational potential of the cluster. The X-ray gas shows a mostly smooth, centrally concentrated distribution of mass. This X-ray emitting gas can also have a significant effect on galaxies as they plunge through the cluster at relatively high velocities ($\sim$1000 km s^{-1}). Ram pressure stripping (Gunn & Gott 1972) and thermal evaporation (Cowie & McKee 1977) act to remove atomic hydrogen from galaxies as bright as L_* on time-scales comparable to a cluster crossing time, which for Coma is at most a few Gyr (Boselli & Gavazzi 2006). Thus, we might expect the star formation history of Coma cluster galaxies to be very different from those that reside outside or on the outskirts of the cluster (Kennicutt, Bothun & Schommer 1984; Donas, Milliard & Laget 1995; Gavazzi et al. 1998, 2010; Cybulski et al. 2014). Indeed, we find strong morphological segregation in Coma, with a large proportion of its members being early-type galaxies (see below). The interstellar medium (ISM) of the cluster late-type galaxies is observed to be affected by the cluster environment (Giovanelli & Haynes 1985; Gavazzi 1989; Casoli et al. 1996; Solanes et al. 2001; Fumagalli et al. 2009; Cortese et al. 2010; Cortese 2012; Boselli et al. 2014), something that is supported by simulation (Tonnesen, Bryan & van Gorkom 2007; Roediger & Brüggen 2008). Gavazzi et al. (2006) found that Coma galaxies are H I-deficient to $\sim$1.5 times the clusters' virial radius, and most H I deficient at the X-ray centre of the cluster. Given this obviously environmental dependence on ISM properties, we will also study here for comparison, along with the Coma cluster galaxies, a sample of galaxies residing in the Great Wall, well beyond the virial radius (defined below) of the cluster.

Although this paper makes use of our optically selected catalogue of Coma (cluster) and Great Wall (filament) galaxies, it is primarily concerned with *Herschel Space Telescope* observations at far-infrared (FIR) wavelengths (see also Bicay & Giovanelli 1987; Contursi et al. 2001; Bai et al. 2006). These FIR observations are predominately measuring emission from relatively cold (10–50 K) cosmic dust. This cosmic dust has been shown to be a good tracer of star formation, molecular material and of metal content and hence galactic chemical evolution, which are themes we explore in this paper.

Due to extinction in the Earth's atmosphere, FIR observations are limited to space-based telescopes. Previously, the first infrared space mission, *IRAS* (Neugebauer et al. 1984), detected 41 sources in Coma as part of its all-sky survey (wavelengths 25–100 μm). The sample was almost entirely composed of late-type galaxies in the periphery of the cluster. Subsequently using *ISO* (Kessler et al. 1996), which extended the FIR wavelength coverage to $\sim$200 μm), Contursi et al. (2001) detected 11 Coma galaxies. They found that even though the galaxies were interacting with the intergalactic medium, their dust properties seemed to be strangely unaffected by this. *ISO*'s extended wavelength coverage also revealed a previously unseen cold dust component ($\sim$10 K), but it was rather poorly constrained because of lack of data beyond 200 μm. The *Spitzer Space Telescope* (Werner et al. 2004) did not extend the wavelength coverage of *ISO*, but it did improve sensitivity. Edwards & Fadda (2011) used *Spitzer* to observe multiple fields in Coma covering a total area of $\sim$3 deg^2, approximately 1/9 of the area traced by the virial radius. They confirmed that star formation was strongly suppressed in Coma's core and observed some starburst galaxies in the south-west, which they identified as a region where galaxies were currently falling into the cluster for the first time.

The above instruments primarily allowed the study of what we would now refer to as warm dust ($T \approx 30$ K). They were limited in their ability to constrain the amount of cold dust ($T < 30$ K) as they did not provide accurate measurements of the Raleigh–Jeans tail of the modified blackbody emission, which typically has been shown to peak at $\sim$160 μm (Davies et al. 2012).

The *Herschel Space Telescope* (Pilbratt et al. 2010) and its instruments were designed to overcome this problem, enabling observations out to about 500 μm and hence a measurement of the total dust content of galaxies. These observations can be used to investigate the issues briefly outlined above.

Previously, Hickinbottom et al. (2014) have published deep *Herschel* observations of 1.75 deg^2 of the Coma cluster core at 70, 100 and 160 μm. We can now extend these observations both spatially and in wavelength range.

The Coma cluster was also observed as part of the *Herschel* Astrophysical Terahertz Large Area Survey (H-ATLAS; Eales et al. 2010), and it is these data we use in this paper. This is the largest *Herschel* FIR extragalactic survey covering 570 deg^2 in five bands centred at 100, 160, 250, 350 and 500 μm. With high Galactic latitudes, the H-ATLAS fields are all located in areas of low galactic cirrus, Coma being part of the Northern Galactic Cap (NGP) field. Along with Coma there is also a wide spatial coverage of the surrounding areas well beyond the cluster's virial radius into its connecting galactic filament.

2 THE OPTICAL SELECTION OF CLUSTER AND FILAMENT GALAXIES

Unlike our previous work on the Virgo (Davies et al. 2014) and Fornax (Fuller et al. 2014) clusters, there is no equivalent optical catalogue of Coma cluster galaxies.[1] Our previous papers on Virgo and Fornax used optical data from the VCC and FCC to distinguish cluster members from background galaxies. The often cited Coma catalogue of Godwin & Peach (1977) is actually just a list of all objects detected on a photographic plate with no additional means of separating cluster from non-cluster galaxies. Specific redshift surveys do exist for various parts of the Coma region (Kent & Gunn 1982; Colless & Dunn 1996; Geller, Diaferio & Kurtz 1999; Castander et al. 2001; Mobasher et al. 2001), but the lack of homogeneity of these surveys precluded the generation of a unified redshift selected Coma Cluster Catalogue (CCC) suitable for our purposes.

However, this region of the sky is now covered by both the spectroscopic and photometric SDSS surveys, and thus allows us to select a clearly defined optical catalogue with secure redshifts. This also enables us to select and isolate both Coma cluster and filament ('Great Wall') galaxies. Our hope is that this CCC will be as useful a tool for studies of nearby galaxies and clusters as both the VCC and FCC have already been.

The SDSS Main Galaxy Sample (MGS) is selected from the spectroscopic survey according to criteria discussed extensively in Strauss et al. (2002). Briefly, objects are selected if they are detected at 5σ or above in the r band. Galaxies are then separated from stars by deciding if they are point or extended sources and also stipulating that they have not been flagged as SATURATED, BRIGHT or BLENDED. Finally, the selected sources must have an r-band apparent magnitude brighter than $m_r = 17.8$.[2] The SDSS spectrograph also had the physical limitation that two fibres could

[1] Similar data to that used here for the combined Coma and A1365 clusters along with galaxies in the 'Great Wall' have previously been described in Gavazzi et al. (2010).

[2] To confirm that the SDSS magnitudes we have used are consistent across the magnitude range, we have checked them against the V-band data available

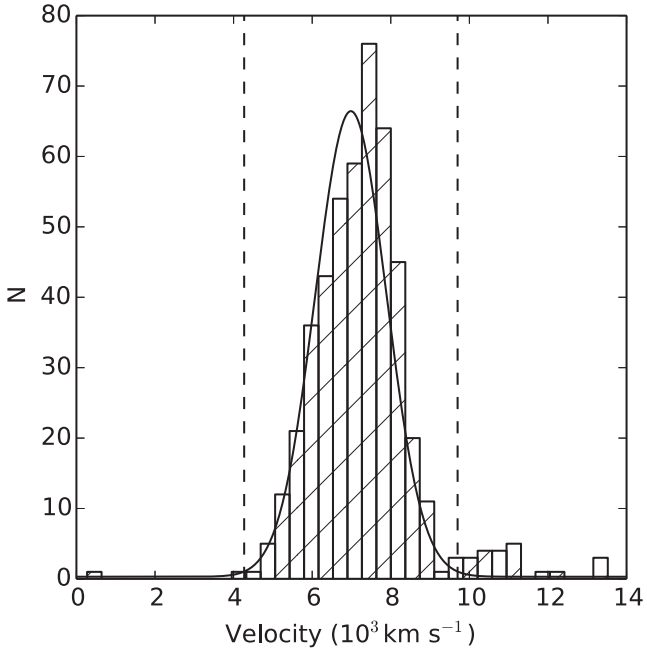

Figure 1. The velocity distribution of the CCC galaxies, showing a clearly relaxed system. The vertical dashed lines represent the 3σ velocity dispersion of the fitted Gaussian function (solid line).

not be closer together than 55 arcsec or ∼28 kpc at a Coma distance of 105 Mpc (Boselli & Gavazzi 2006), but this was not a problem for the bright Coma cluster galaxies considered here ($m_r = 17.8$ corresponds to an absolute magnitude of ≈−17.3 at the above Coma distance). Our sample is selected from the MGS (SDSS DR10) by isolating the cluster and filament in both spatial and velocity extent.

Our initial selection was for all galaxies within a velocity range 3000–11 000 km s^{-1}, with a spatial selection over the area of the *Herschel* NGP field. The velocity range is roughly symmetrical about the current value for Coma's mean velocity as listed in the NASA/IPAC Extragalactic Database[3] of ∼7000 km s^{-1}.

2.1 Defining the cluster

Many clusters are far from virial equilibrium and so R_{200}, the radius at which the mass density drops to 1/200 of the critical density, is often used as a measure of their size. Coma however appears to be a dynamically mature cluster, making the virial radius a less arbitrary choice in this particular case. A cluster in virial equilibrium would have a velocity distribution perfectly traced by a Gaussian function. Fig. 1 (details below) shows that this is a good interpretation of the Coma data.

We have defined the centre of Coma as the position of peak X-ray emission (Colless & Dunn 1995). This X-ray emitting gas is a much more reliable indicator of the mass distribution of the cluster than the optical surface density of galaxies, as it better traces the total mass distribution. Using this definition, we measure the centre to be at RA(J2000) = $12^h59^m48\overset{s}{.}7$ and Dec.(J2000) = $+27^\circ58'50\overset{''}{.}0$. From the literature, we have found four different derived values for the virial radius of Coma (The & White 1986; Hughes 1989; Geller et al. 1999; Kubo et al. 2007). After adjusting to a common distance scale ($H_0 = 70$ km s^{-1} Mpc^{-1}), we have used the mean of these four values for the virial radius, i.e. 3.1 ± 0.7 Mpc.

Table 1. Derived parameters of the Coma cluster.

Virial radius	3.1 Mpc
Velocity dispersion, σ	905 km s^{-1}
Mean cluster velocity, μ	6984 km s^{-1}
Minimum velocity limit, $\mu - 3\sigma$	4268 km s^{-1}
Maximum velocity limit, $\mu + 3\sigma$	9700 km s^{-1}

We define a velocity selection similar to the VCC's (Binggeli et al. 1985), i.e. using the velocity dispersion (σ) of a Gaussian function fitted to galaxies within the projected virial radius. However, this velocity dispersion is sensitive to the initial 'rough' velocity selection used (see above). In order to overcome this problem, we have used an iterative method to define the cluster population. We fit a Gaussian function to the velocity data, then remove galaxies that are outside of 3σ and then re-fit the Gaussian function until the value for σ converges.

Figs 1 and 2 indicate that this is an appropriate method for defining the cluster galaxies. The goodness of fit of a Gaussian to the histogram of velocities gives $\chi^2_{\rm dof\,=\,23} = 30.1$ (where $\chi^2_{\rm dof\,=\,23} = 35.2$ is equivalent to a 95 per cent confidence interval). Both in front of and behind the cluster there are natural voids that help to define the cluster sample galaxies. Table 1 shows the limits we have used to define the extent of the Coma cluster.

There are 774 SDSS galaxies spectroscopically confirmed within these limits, and these galaxies are henceforth referred to as members of the CCC. The galaxies are listed in Appendix A1 of the online material.

2.2 Defining the filament

The Coma cluster sits within a filamentary structure, which is an overdensity of galaxies that connects it with numerous other groups and clusters. Defining a 'filament' sample is a rather subjective process because unlike the Coma cluster it is clearly a non-virialized structure. However, within the filament there are numerous loose groupings and a range of galaxy densities, making it an interesting region to compare with the cluster sample. Fig. 2 clearly shows that the filament that the cluster sits within, the overdensity at ∼7000 km s^{-1}, extends well beyond 18 Mpc (∼$6R_{\rm virial}$). These are galaxies at about the same recessional velocity as Coma, but spread in a linear structure across the sky. We define the filament sample as any galaxy that falls within the bounds of the NGP survey area, but outside the Viral radius of Coma. In addition, each selected galaxy must satisfy the same velocity criteria, i.e. $4268 < v < 9700$ km s^{-1} as our Coma cluster sample. This yields 951 filament galaxies, which we will refer to as the Coma Filament Catalogue (CFC). The galaxies are listed in Appendix B1 of the online material.

2.3 The *Herschel* data

The NGP field is part of the *Herschel* H-ATLAS survey (Eales et al. 2010). It covers approximately 15° × 10°, centred at RA(J2000) = $13^h18^m00\overset{s}{.}0$, Dec.(J2000) = $+29^\circ00'00\overset{''}{.}0$. The survey field is shown in Fig. 3 along with the positions of the galaxies selected as part of the CCC and CFC samples.

The H-ATLAS survey consists of parallel scan map data from the PACS instrument (Poglitsch et al. 2010) at 100 and 160 μm and

through GOLDMINE. We find a good one-to-one linear relationship across the whole range of magnitudes used.

[3] http://ned.ipac.caltech.edu

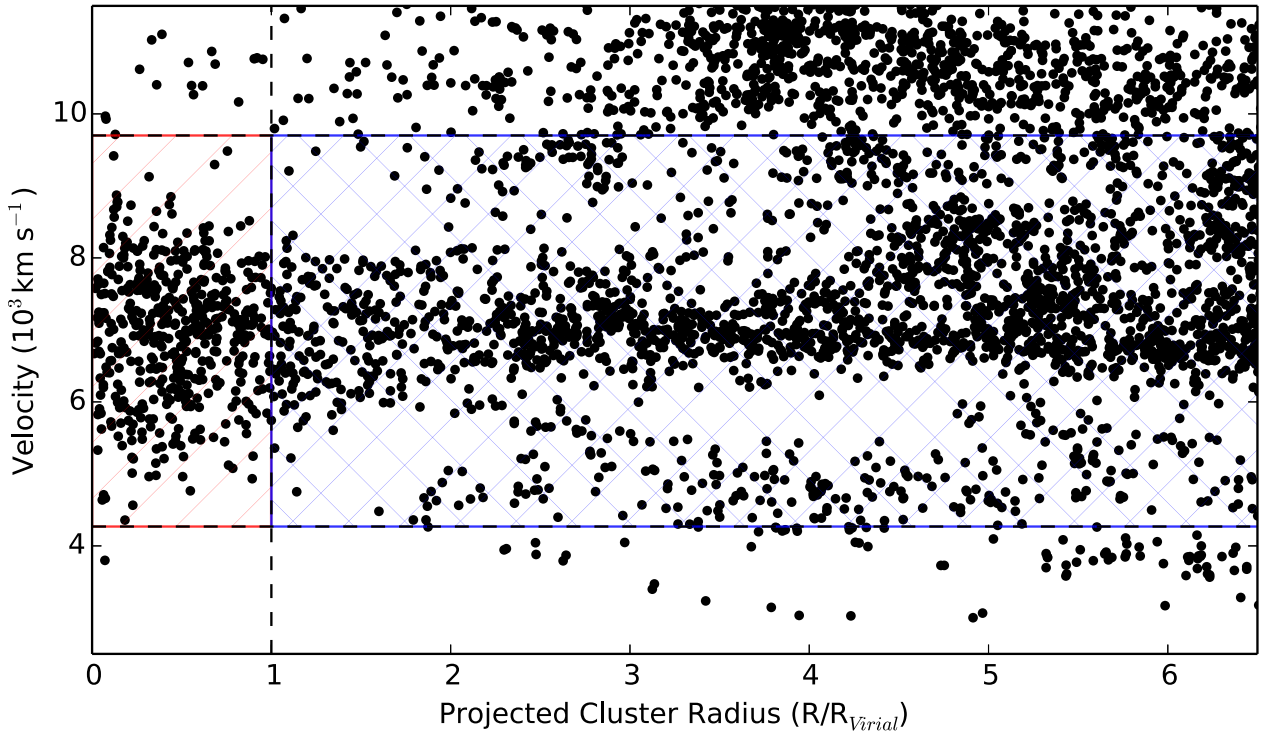

Figure 2. The velocities of galaxies in the Coma cluster region plotted against distance from the Coma cluster X-ray centre (RA(J2000) = $12^h59^m48\overset{s}{.}7$ and Dec.(J2000) = $+27°58'50\overset{''}{.}0$). The red diagonally hatched box is a visual representation of the cluster selection, and the blue cross-hatched box shows the region selected for the filament sample. The filament structure is well defined out to and beyond six times the cluster virial radius. There are reasonably well defined voids in front of and behind the cluster.

the SPIRE instrument (Griffin et al. 2010) at 250, 350 and 500 μm. The PACS data were processed using an updated version of the pipeline presented in Ibar et al. (2010) that now scans the data to identify timeline jumps and glitches (see Valiante et al., in preparation). Then the two scans were combined using the *Scanamorphous* map maker (Roussel 2013). The SPIRE data were processed with a customized pipeline, which is very similar to the official pipeline with the exception that we used a method called BriGAdE (Smith et al., in preparation), in place of the standard temperature drift correction. BriGAdE effectively corrects all the bolometers for thermal drift without removing large extended structures like Galactic cirrus. The two scans were then combined using the mapping software in the standard *Herschel* pipeline.

The final NGP maps have pixel sizes of 3, 4, 6, 8 and 12 arcsec and 1σ noise measured over the entire image of 0.8, 1.1, 0.9, 0.9 and 1.1 mJy pixel^{-1} (or 24.0, 43.8, 11.3, 11.6 and 12.4 mJy beam^{-1}) for 100, 160, 250, 350 and 500 μm, respectively. Beam sizes are of order 2–3 times the pixel size so at the distance of Coma, where 10 arcsec $\simeq$5 kpc, we have the potential to crudely resolve some of the larger galaxies. For example, the two biggest galaxies in the cluster are NGC 4839 and 4889 with optical diameters (D_{25}) of 3.6 and 3.3 arcmin, respectively.

2.4 Comparison with HeViCS and HeFoCS

Below we will compare the Coma *Herschel* data with that previously published by us on the Virgo (Davies et al. 2014) and Fornax (Fuller et al. 2014) clusters. These data were obtained as part of the *Herschel* Virgo Cluster Survey (HeViCS) and the *Herschel* Fornax Cluster Survey (HeFoCS). The FIR maps of all three surveys were created using identical data reduction techniques. However, they differ with respect to depth and spatial coverage of the clusters.

First, we consider the depth of the three surveys. The HeViCS maps consist of eight scans (four pairs of orthogonal cross-linking scans), which is two and four times as many scans as the HeFoCS and H-ATLAS data, respectively. For detector random Poisson noise, we would expect $\sim\sqrt{2}$ and $\sim\sqrt{4}$ increase in instrumental noise in the latter two surveys compared to HeViCS. However, Auld et al. (2013) calculated separately the instrumental and confusion noise and showed that the HeViCS SPIRE bands were effectively confusion noise limited (70 per cent of the overall noise is from confusion at 250 μm). Consequently, when planning the HeFoCS survey, only four scans were requested as this produced confusion limited maps with half the time required for a single HeViCS tile. The H-ATLAS (NGP) survey was designed to cover as much area as possible and consequently with its two scans does not reach the confusion noise at 250 μm.

In order to measure the ratio of the global noise in the HeViCS, HeFoCS and H-ATLAS NGP maps, we measure the pixel–pixel fluctuations and apply an iterative 3σ clip to remove bright sources. The measured 'global' noise in the HeViCS, HeFoCS and NGP at 250 μm is 7.5, 8.9 and 11.3 mJy beam^{-1}, respectively. Yielding measured noise ratios between the HeViCS and HeFoCS and HeViCS and NGP of 1.2 and 1.5, respectively, i.e. not simple Poisson noise because of the constant contribution of source confusion – thus the surveys are better suited for comparison than initial expectation.

Secondly, we consider the coverage of the HeViCS, HeFoCS and NGP FIR maps of their respective clusters. The Coma cluster is covered well beyond the virial radius; however, calculating the coverage for the other surveys is less straightforward. The clusters have very different physical sizes and states of relaxation – Virgo is

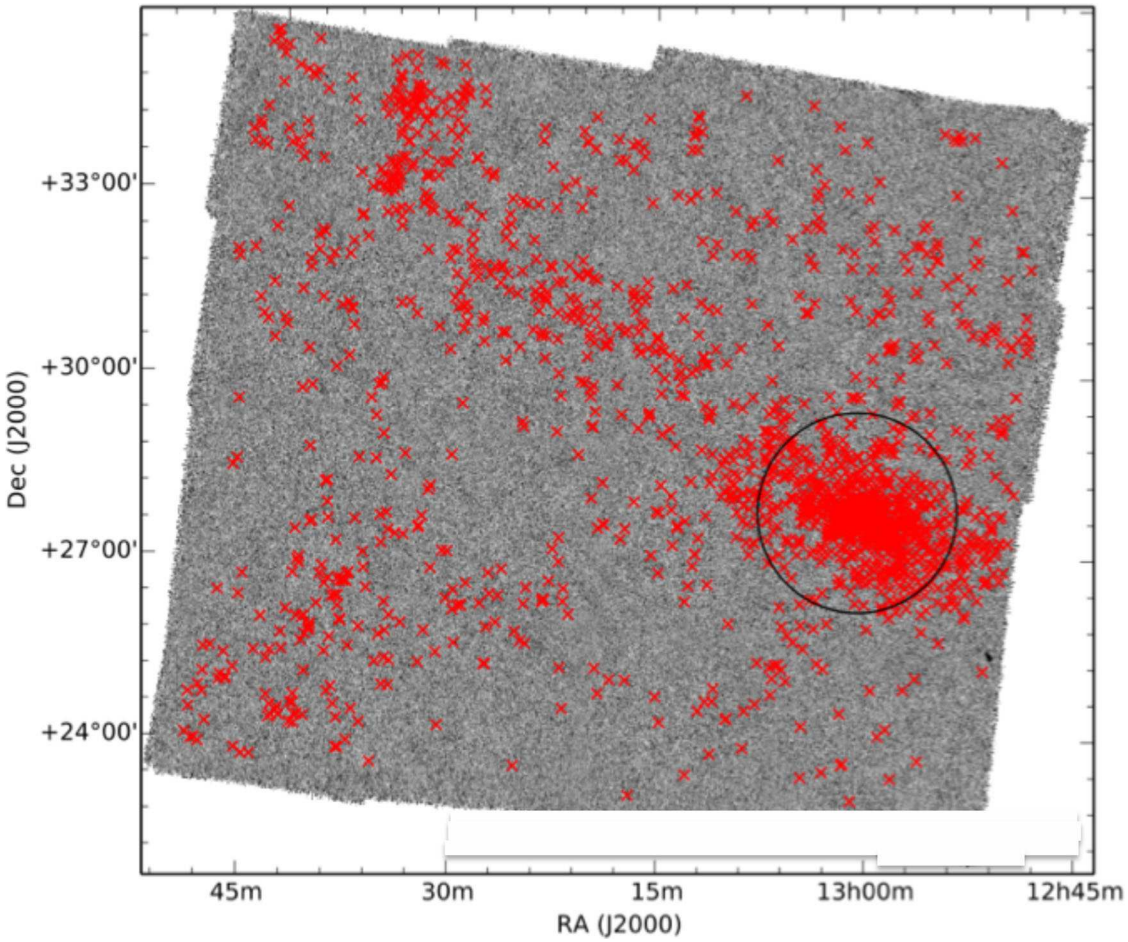

Figure 3. The area of sky covered by the H-ATLAS NGP map. The red crosses mark the position of galaxies in both our cluster (CCC) and filament (CFC) samples. The black circle marks the approximate position of the 1.°7 or 3.1 Mpc virial radius of the cluster.

far more 'clumpy' than Fornax or Coma (Davies et al. 2014). The HeViCS FIR maps consist of four tiles each of $4^\circ \times 4^\circ$ running north to south (Davies et al. 2012), whereas the HeFoCS is only a single tile of $4^\circ \times 4^\circ$ (Fuller et al. 2014). Virgo and Fornax are at about the same distance from us (∼17 Mpc), but Fornax is physically much smaller than Virgo (by about a factor of 4). However, the *Herschel* data do include about the same fraction of VCC and FCC galaxies – about two-third of them in both cases. Of course, more problematic when comparing the properties of the clusters is the more than five times greater distance to Coma than to either Virgo or Fornax – this and the relevant areas covered by the three surveys will be discussed further below.

2.5 Flux measurement

2.5.1 General approach

We have used a semi-automated flux measurement program, to measure the FIR flux density of each galaxy in the CCC and CFC. This program is fully described and extensively tested by Auld et al. (2013). The method is briefly described below.

The optical parameters (position, eccentricity, optical diameter D_{25} and position angle) from the optical catalogues were used to make an initial estimate of the shape and size of the FIR emission. Previous studies (Cortese et al. 2010; Pohlen et al. 2010) show that FIR emission is well traced by the optical parameters of late-type galaxies, whereas early-type galaxies typically show more compact dust emission (Smith et al. 2012). The optical parameters are only used to make an initial estimate for creating masks. The program then iterates, to create new masks and apertures (of the same size for each FIR band) that best match the diameter and ellipticity of the FIR emission. The following explanation of the process relates to the information shown in Fig. 4.

The flux measurement process starts by extracting a 200×200 pixel sub-image from the raw map as shown in Fig. 4(b). To measure the background of the sub-image, all nearby galaxies including the galaxy being measured are initially masked at $1.5 \times D_{25}$. If the optical extent of the galaxy is such that this sub-image is not large enough to give an accurate background estimation, then the program will increase the size of the sub-image, up to 600×600 pixels for SPIRE and 1200×1200 pixels for PACS data.

The background estimation has to deal with the near confusion limited SPIRE maps and instrumental noise in the PACS maps. The program was originally written for use with the HeViCS maps where Galactic cirrus was also a major problem. In order to remove bright background galaxies and galactic cirrus, Auld et al. (2013) used a 98 per cent flux clip and then fitted the remaining pixels with a 2D polynomial. The flux clip removes bright background galaxies by masking out the brightest 2 per cent of pixels; this ensures that the 2D polynomial is only fitting the background. Unlike the Virgo fields, cirrus is not obviously present in the NGP maps and so the

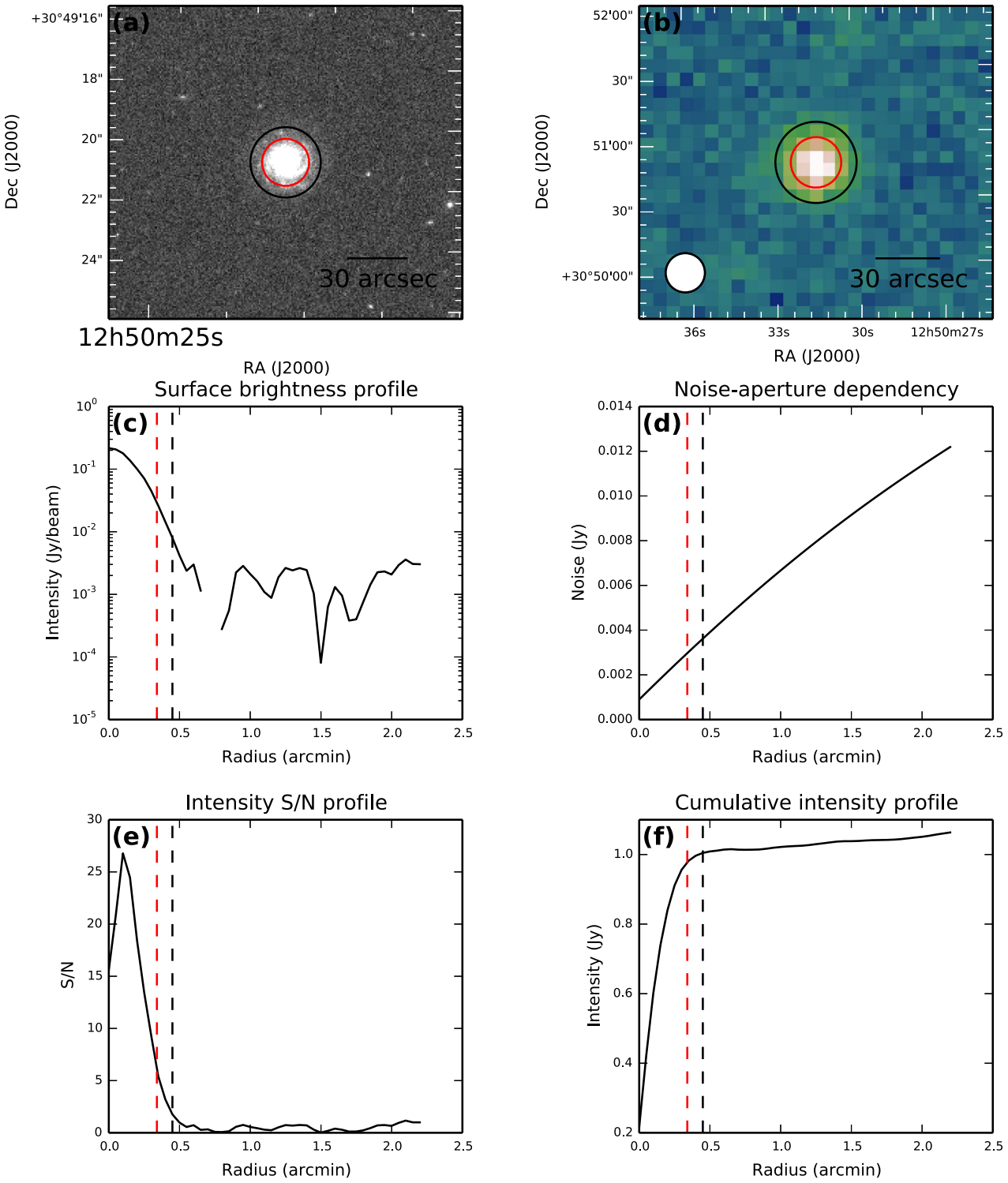

Figure 4. An example of the output generated for each detected CCC and CFC galaxy after we have carried out our automated photometry. Excluding the upper-left panel, all panels refer to the *Herschel* 250 μm band. (a) An optical image of the galaxy, the red and black ellipses show the optical D_{25} and the FIR extent of the galaxy (see the text for definition). (b) The raw sub-image cutout of the FIR map. The beam size is shown in the lower-left corner. (c) The surface brightness profile. (d) Noise for an equivalent sized circular aperture (see the text for definition). (e) S/N per annuli. This shows the cut-off when S/N ≤ 2. (f) A cumulative intensity profile. The red and black dashed lines show the optical and FIR extent, respectively.

98 per cent clip is retained, but then we just use the median pixel value of the masked sub-image as the background value.

For each detected source, we measure total flux, surface brightness, aperture noise (fully described in Section 2.5.2) and signal-to-noise (S/N) around annuli of increasing radii centred on the galaxy's optical centre. The shape of the annuli is based on the galaxy's optical parameters convolved with the appropriate point spread function (PSF). As an example, we plot the corresponding radial profiles in

Figs 4(c), (e) and (f), respectively. The FIR diameter[4] $D_{\rm FIR}$ is defined where the S/N profile drops below 2. This $D_{\rm FIR}$ is used to replace the $1.5 \times D_{25}$ used to make the initial mask. The process iterates until the mask and the $D_{\rm FIR}$ value converge. We then applied an aperture correction as given in Ibar et al. (2010) – this takes account of the encircled energy fraction within the chosen aperture size.

For objects where the total S/N value was less than 3, the sub-image was searched for a point source. After convolving with the relevant wavelength-dependent PSF, the maximum pixel value within the full width at half-maximum (FWHM) of the PSF centred on the optical position was taken as the flux. The noise was calculated according to Marsden et al. (2009) and Chapin et al. (2011). This involves plotting a histogram of all the pixel values in the PSF-convolved sub-image and fitting a Gaussian function to the negative tail. The FWHM of this Gaussian is then used to estimate the combined instrumental and confusion noise. This has been summed in quadrature with the calibration uncertainty (see below) to obtain a value for the total noise. If the S/N was still less than 3, we consider the object undetected and set an upper limit on the flux equal to three times the noise in the PSF-convolved sub-image. So, for the optically selected galaxies that do not have an FIR detection, we have set an upper limit on their FIR flux density equal to the 3σ noise from the PSF-convolved map. This marked the end of the automatic source measurement process. The output is in the form of data files for each galaxy and the visual output shown in Fig. 4. Tables A1 and B1 in the appendices list flux measurements (or lack of) for all galaxies in the CCC and CFC samples.

2.5.2 Total error estimate

The total error on each flux density measurement is estimated from the calibration uncertainty, $\sigma_{\rm cal}$ and aperture uncertainty, $\sigma_{\rm aper}$, summed in quadrature.

For SPIRE, $\sigma_{\rm cal}$ is based on single scans of Neptune and on an assumed model of its emission. The final error for each band is estimated to include 4 per cent correlated and 1.5 per cent from random variation in repeated measurements. The SPIRE observer's manual[5] suggests that these should be added together, leading to a SPIRE $\sigma_{\rm cal}$ of 5.5 per cent.

For PACS, $\sigma_{\rm cal}$ is based on multiple sources with different models of emission. The PACS observer's manual[6] lists the uncorrelated uncertainties as 3 and 4 per cent for 100 and 160 μm, respectively, and the correlated uncertainty is given for point sources as 2.2 per cent. However, the data used for calculating these uncertainties were reduced and analysed in a different way to our data. Auld et al. (2013) considered this problem and concluded that there was about a 12 per cent calibration uncertainty, which is the value we adopt here.

To calculate the aperture uncertainty ($\sigma_{\rm aper}$), a large number of apertures of a fixed size were placed randomly on each sub-image. We measure the total flux in each aperture, then by applying an iterative 3σ clipping procedure use σ as the uncertainty for that aperture. Repeating this for a range of aperture sizes allows us to estimate the aperture uncertainty as a function of size. This method takes into account both confusion noise and instrumental noise. Fig. 4(d) shows a plot of aperture noise against radial distance.

2.5.3 Dealing with blending and contamination

Herschel's comparatively large beam size can lead to unavoidable contamination by FIR background sources, which could be falsely identified with the optical source. Due to the distance of Coma, many of the CCC and CFC galaxies are point rather than extended detections in the *Herschel* data. Thus, 'by-eye' inspection to reject background sources is more ambiguous than it was for the HeViCS and HeFoCS. However, the comparatively large survey area allows us to use a 'Monte Carlo' method to model the expected contamination for a given FIR–optical source separation. We will assume that if extended emission is detected at the location of an optical Coma galaxy, it is a reliable detection. Consequently, the following discussion only applies to the point source population, which is ∼60 per cent of the total detections at 250 μm.

As was done for HeViCS and HeFoCS, we impose a strict criterion that a galaxy must be detected at 250 μm to be included as a *Herschel* FIR detection – 250 μm provides the best combination of sensitivity and resolution (see below). Thus, we estimate the contamination at 250 μm. We have done this by comparing the measured separation between an optically detected galaxy in our catalogue and an FIR detected source, with that for a random catalogue of equal size.

We have computed the distance from the optical source to the nearest FIR neighbour using the North Galactic Point Source Catalogue (NGPSC).[7] The white diagonally hatched histogram in the upper panel of Fig. 5 shows the distribution of nearest-neighbour separations. Clearly, quite a lot of CCC/CFC optically selected galaxies have an FIR source within ∼2 arcsec. We have then repeated this process, using a catalogue of equal length to the CCC/CFC, but with random positions on the sky. In order to minimize the error in this latter step, we repeat this random catalogue generation and cross-match many ($\sim 10^6$) times. The random-NGPSC separation distance distribution is shown as a blue histogram in the upper panel of Fig. 5 – it is little difficult to see because the numbers are small over these angular separations, but this does indicate that contamination is not a major problem. The association of optical and FIR sources is clearly very different if the optical galaxies are laid down at random. Combining the above two results, the lower panel of Fig. 5 shows the percentage contamination in our catalogue for each bin of angular separation. We have then fitted a third-order polynomial using a χ^2 minimization technique and calculated the angular separation where the contamination is equal to 5 per cent, we find this to be at ∼4 arcsec. Given that our pixel size at 250 μm is 6 arcsec, we are essentially requiring that the FIR source position corresponds with the optical source position to plus or minus one 250 μm pixel.

2.6 Flux verification

In order to verify our automated FIR source measurement process, we cross-match and compare our measured fluxes with FIR data from the literature. The result is shown in Fig. 6 with gradients and intercepts tabulated in Table 2. We matched our catalogue with the *IRAS* point source catalogue (Helou & Walker 1988), the *IRAS*

[4] As many galaxies are not resolved, $D_{\rm FIR}$ in this case will be defined by the PSF of the *Herschel* beam and will not be representative of the extent of dust in the galaxy.

[5] http://herschel.esac.esa.int/Docs/SPIRE/html/spire_om.html

[6] http://herschel.esac.esa.int/Docs/PACS/html/pacs_om.html

[7] The NGPSC is a list of *Herschel* 250 μm detections in the NGP field (Valiante et al., in preparation).

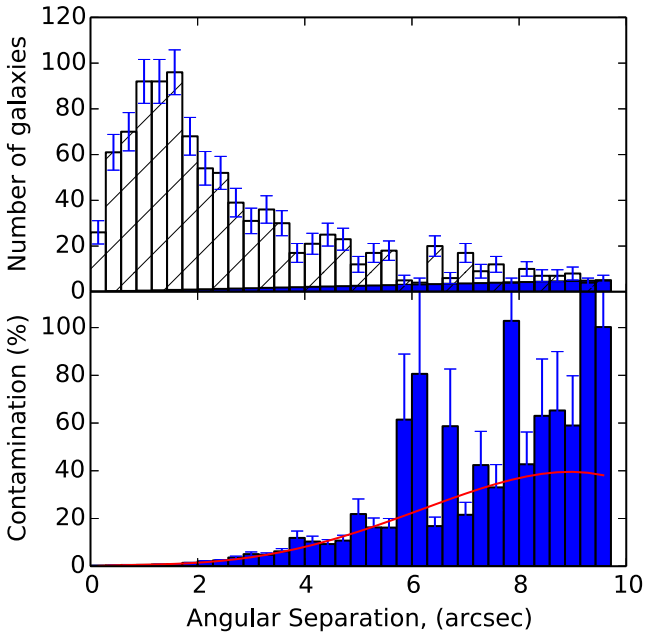

Figure 5. The results of our simulations and our method for estimating possible contamination by background sources at 250 μm. The clear hatched histogram in the upper panel shows the distribution of angular separations of optically detected CCC/CFC galaxies from their nearest FIR detected neighbour. The blue histogram in the upper panel (most easily seen in the bottom-right corner) shows the mean distribution of our simulations of a random catalogue of galaxies. The lower panel shows the contamination for each bin of angular separation. The red line is a third-order polynomial fitted to the data using a χ^2 minimization technique.

faint source catalogue (Conrow et al. 1993), Hickinbottom et al. (2014) a deep *Herschel* PACS survey of the Coma cluster core and with the NGPSC data. Table 2 shows overall that the results are consistent with a gradient of unity and an intercept of zero. However, the faintest (<50 mJy) matched sources from Hickinbottom et al. (2014) appear brighter than the flux recorded at 100 and 160 μm in our catalogue. These sources were all recorded at fluxes below the 3σ global noise limit of the NGP PACS maps. After extensive testing by both ourselves and Hickinbottom et al., we have placed a further criterion for a source to be detected in the PACS bands, i.e. we require all PACS sources to have a flux density greater than three times the global measured noise in the NGP PACS maps before we record it as a detection. Flux density or upper limit values are given for all CCC and CFC galaxies in Appendices A and B of the online material.

3 SPECTRAL ENERGY DISTRIBUTION FITTING

As in Davies et al. (2012), we have fitted a modified blackbody to every galaxy detected in all five *Herschel* bands (198 galaxies) using the following function:

$$S_\lambda = \frac{\kappa_{\rm abs}(\lambda) M_{\rm dust} B(\lambda, T_{\rm dust})}{D^2}, \quad (1)$$

where S_λ is the flux density at wavelength λ, $M_{\rm dust}$ is the dust mass, $T_{\rm dust}$ is the dust temperature, $B(\lambda, T_{\rm dust})$ is the Planck function, D is the distance to the cluster (105 Mpc) and $\kappa_{\rm abs}$ is the dust absorption

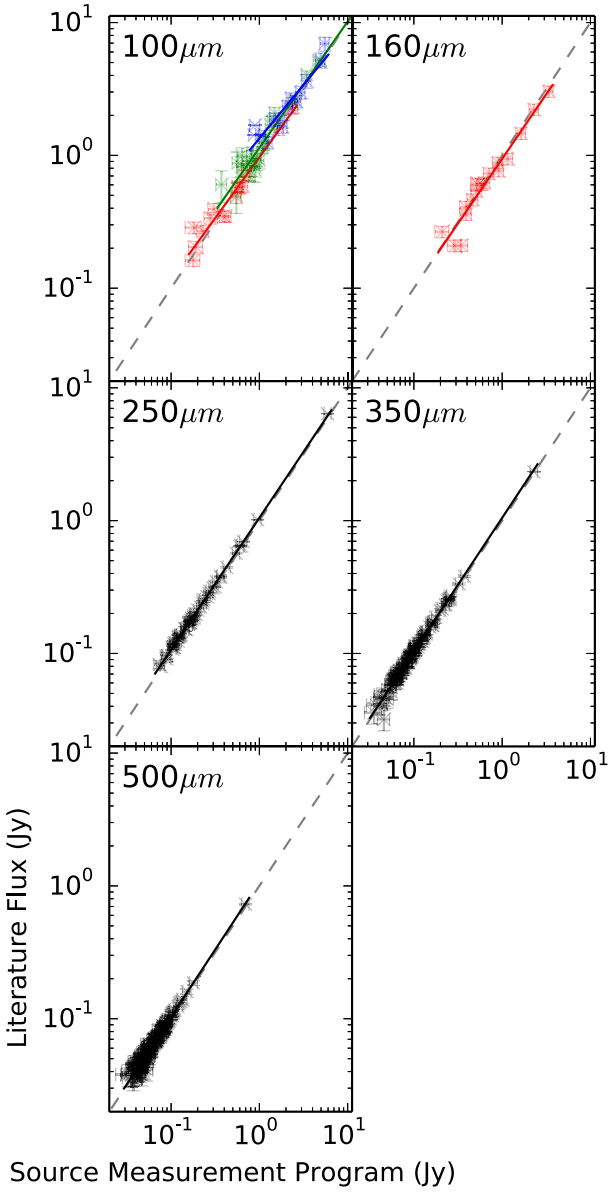

Figure 6. The FIR CCC/CFC fluxes plotted against other measured values. Markers are as follows: *IRAS* faint source catalogue (Conrow et al. 1993), green; *IRAS* point source catalogue (Helou & Walker 1988), blue; deep PACS (Hickinbottom et al. 2014), red; and NGPSC, black. The grey diagonal dashed line represents a linear exact relation, i.e. $y = mx + c$, where $m = 1$ and $c = 0$.

Table 2. The parameters of the straight line fits shown in Fig. 6.

Band (μm)	Gradient, M	Intercept, C
100[a]	1.06 ± 0.01	0.07 ± 0.04
100[b]	1.09 ± 0.08	0.11 ± 0.21
100[c]	0.92 ± 0.06	0.03 ± 0.02
160[c]	0.95 ± 0.08	0.02 ± 0.04
250[d]	1.07 ± 0.01	−0.01 ± 0.06
350[d]	1.02 ± 0.02	−0.01 ± 0.02
500[d]	1.00 ± 0.03	0.01 ± 0.02

[a]IRAS FSC – Conrow et al. (1993)
[b]IRAS PSC – Helou & Walker (1988)
[c]Deep PACS – Hickinbottom et al. (2014)
[d]NGPSC

Table 3. The tables show the availability of metallicity and H I data for the CCC/CFC galaxies split by morphological type (see the text for details). The numbers in parentheses refer to the percentage of that galaxy for a given morphological type.

Sample	N_{late}	$N_{uncert.}$	N_{early}	N_m
CCC/CFC	474	963	288	1725
CCC/CFC (+Metallicity)	285 (60%)	295 (30%)	5 (1%)	585 (33%)
CCC/CFC (+H I)	119 (25%)	81 (8%)	8 (2%)	208 (12%)

Sample	Cluster			Filament		
	N_{late}	$N_{uncert.}$	N_{early}	N_{late}	$N_{uncert.}$	N_{early}
CCC/CFC	83	504	187	391	459	101
CCC/CFC (+Metallicity)	25 (30%)	53 (11%)	1 (<1%)	260 (67%)	242 (53%)	4 (4%)
CCC/CFC (+H I)	24 (29%)	21 (4%)	7 (4%)	95 (24%)	60 (13%)	1 (1%)

coefficient. The latter follows a power law modified by an emissivity (β), such that

$$\kappa_{abs}(\lambda) = \kappa_{abs}(\lambda_0) \times \left(\frac{\lambda_0}{\lambda}\right)^{\beta}. \quad (2)$$

We assume that emission at these wavelengths is purely thermal and from dust at a single temperature with a fixed $\beta = 2$ emissivity (Davies et al. 2012). We use $\kappa_{abs}(350\,\mu m) = 0.192\ m^2\ kg^{-1}$ according to Draine (2003). The above function is fitted using a χ^2 minimization technique.

Although this is most likely an overly simplistic analysis, this approach has been used in previous works (Davies et al. 2010, 2012; Smith et al. 2012; Auld et al. 2013; Verstappen et al. 2013) and shown to fit the data very well in the FIR/sub-mm regime. Bianchi (2013) showed that using a single-component modified blackbody returns equivalent results to more complex models such as those described in Draine & Li (2007). From our fits, we obtain dust masses and temperatures. Spectral energy distribution (SED) data and modified blackbody fits are shown in Appendix D, and 250 μm images in Appendix C of the online material.

4 AUXILIARY DATA

In this section, we describe additional available data that we can make use of in our subsequent analysis. As described above, the H-ATLAS NGP region is covered by the SDSS spectroscopic and photometric surveys, which provides not only the positions, magnitudes, sizes and shapes as used above, but also star formation rates (SFRs), stellar mass and metallicity for a significant fraction of our detected objects. We will also take advantage of available atomic gas data.

4.1 Stellar mass, SFR and metallicity

Brinchmann et al. (2004) [see also Kauffmann et al. (2003) and Tremonti et al. (2004) who have carried out photometry and spectral analysis, respectively, for the same sample] have used SDSS spectra and optical colours to calculate stellar mass,[8] SFR and gas phase metallicities for galaxies that reside in the NGP area. Below we will use these data as part of our analysis of the galaxies in our FIR sample. Brinchmann et al. (2004) designate a galaxy as either having emission lines or not. For galaxies without emission lines, stellar masses and SFRs are calculated using the optical colours and the 4000 Å break in the SDSS spectra. However, galaxies without emission lines do not have measured metallicities. In Table 3, we indicate the number of galaxies in the CCC/CFC with and without measured metallicities – morphologies are defined in Section 4.3.

4.2 Atomic hydrogen

We have cross-matched the CCC/CFC with data collected by Gavazzi et al. (2006) and for galaxies in the Arecibo Legacy Fast Arecibo L-band Feed Array Survey (ALFALFA; Haynes et al. 2011). Gavazzi et al. (2006) used the Arecibo radio telescope to observe 35 spiral galaxies in the Coma supercluster. They also added all data then available in the literature, giving 92 galaxies in total. The ALFALFA 0.4α data (Haynes et al. 2011) add a further 138 galaxies to this. So, in total we have atomic hydrogen data for 230 CCC/CFC galaxies. Where we have a measurement from both the literature and from ALFALFA we have taken the value from ALFALFA 0.4α. In Table 3, we give the numbers of galaxies detected in H I of each morphological type (see below) in the cluster and filament.

4.3 Morphology

The larger distance of the Coma cluster makes morphological classification far more ambiguous, especially for the fainter members of the CCC/CFC, than that for both Virgo and Fornax galaxies. The Galaxy Zoo project (Lintott et al. 2008) covers the majority of the SDSS DR7 galaxies that are included in the spectroscopic sample. They invite members of the general public to decide if a galaxy is either an elliptical or spiral. Based on these votes, each galaxy can then be assigned a probability of being elliptical p(E) or spiral p(S). This allows us to define three morphological categories: early, $p(E) > 0.8$; late, $p(S) > 0.8$ and uncertain where $p(E) < 0.8$ and $p(S) < 0.8$. We will discuss the significance of these morphological categories below.

The GOLDMINE data base (Gavazzi et al. 2003) provides multi-wavelength data from a number of sources, with varying levels of completeness. As part of the GOLDMINE data base, Gavazzi & Boselli (1996) catalogued galaxies in the Coma region. They are complete for galaxies in the B-band brighter than $m_B = 15.5$, covering a large – although not total – fraction of the NGP survey area. They visually classify galaxy morphologies into the more familiar Hubble types (E through to Sd). However, the brighter magnitude limit and reduced area coverage mean that only 256 (15 per cent) galaxies are in both GOLDMINE and our CCC/CFC catalogues.

[8] In order to make the stellar masses in Coma consistent with our previous Fornax (Fuller et al. 2014) and Virgo (Davies et al. 2014) papers, we have adjusted the SDSS stellar masses by +0.15 dex to convert from the Kroupa initial mass function (IMF; Kroupa 2002) to a 'diet' Salpeter IMF (Bell et al. 2003) as per the recipes in Brinchmann et al. (2004).

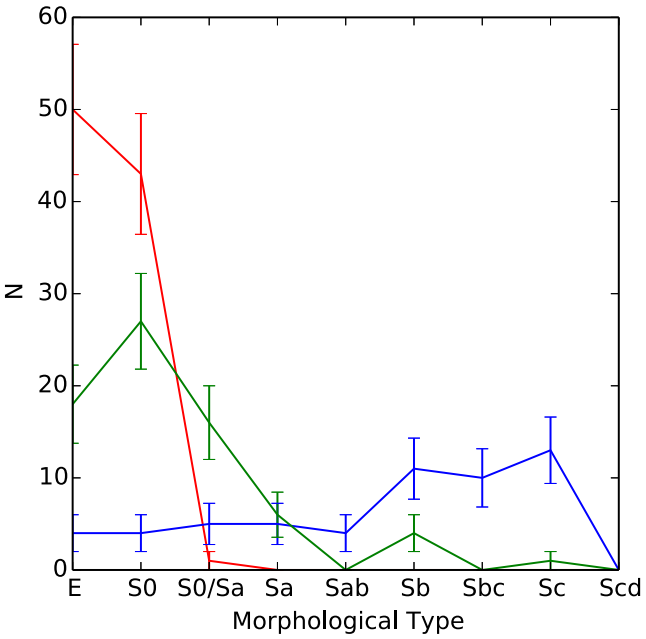

Figure 7. Histograms of morphology assignments from the GOLDMINE data base (*x*-axis) in each of our morphological groups from the Galaxy Zoo: early-type (red), uncertain (green) and late-type (blue). The error bars are simply root *N*.

The Galaxy Zoo catalogue has been shown to be consistent with classifications of the same galaxies by professional astronomers (Lintott et al. 2008). However, Lintott et al. (2008) also show that fainter galaxies are harder to classify and more likely to be classified as an early-type or uncertain-type. In order to understand our three morphological groups, based upon the above selection, we compare our classification with that of GOLDMINE – Fig. 7.

Fig. 7 clearly shows that at the distance of Coma, Galaxy Zoo is a good predictor of morphology when compared to GOLDMINE. Early-types with a 0.8 likelihood selection are mainly composed of E and S0's (∼98 per cent), and only one early-type is in the S0/Sa bin. Late-type galaxies are mainly composed of Sa to Sc's types. However, eight galaxies are classified as late-type by Galaxy Zoo and early-type by GOLDMINE. In order to understand this, we have visually inspected these galaxies (see Fig. 8). Four of these galaxies (CCC 232, CCC 513, CFC 57 and CFC 344) are clearly edge-on galaxies, and as such morphological classification is always ambiguous. The remaining four galaxies are clearly late-types and so appear to be misclassified in GOLDMINE.

Fig. 7 also helps us understand the morphological make-up of the uncertain-type. The uncertain-type covers a range of morphologies from E to Sc; however, it is mostly made up of S0 and S0/Sa galaxies.

4.4 Local density

In order to examine the effect of local structure or environment rather than large-scale structure such as the cluster and filament, we simply use the *N*th nearest-neighbour statistic (Σ_N) as defined by the equation

$$\Sigma_N = \frac{N}{\pi D_N^2} \tag{3}$$

to measure the local density of optically selected CCC/CFC galaxies. Σ_N is the surface density out to the *N*th nearest neighbour that lies at a distance D_N. As we assume that all our galaxies are at ∼100 Mpc, we effectively 'collapse' our catalogues of cluster and filament galaxies into a 2D plane and measure spatial distances on the sky.

We have calculated Σ_N for the 1st, 5th and 10th nearest neighbours for each galaxy. In order to avoid edge effects for this analysis,

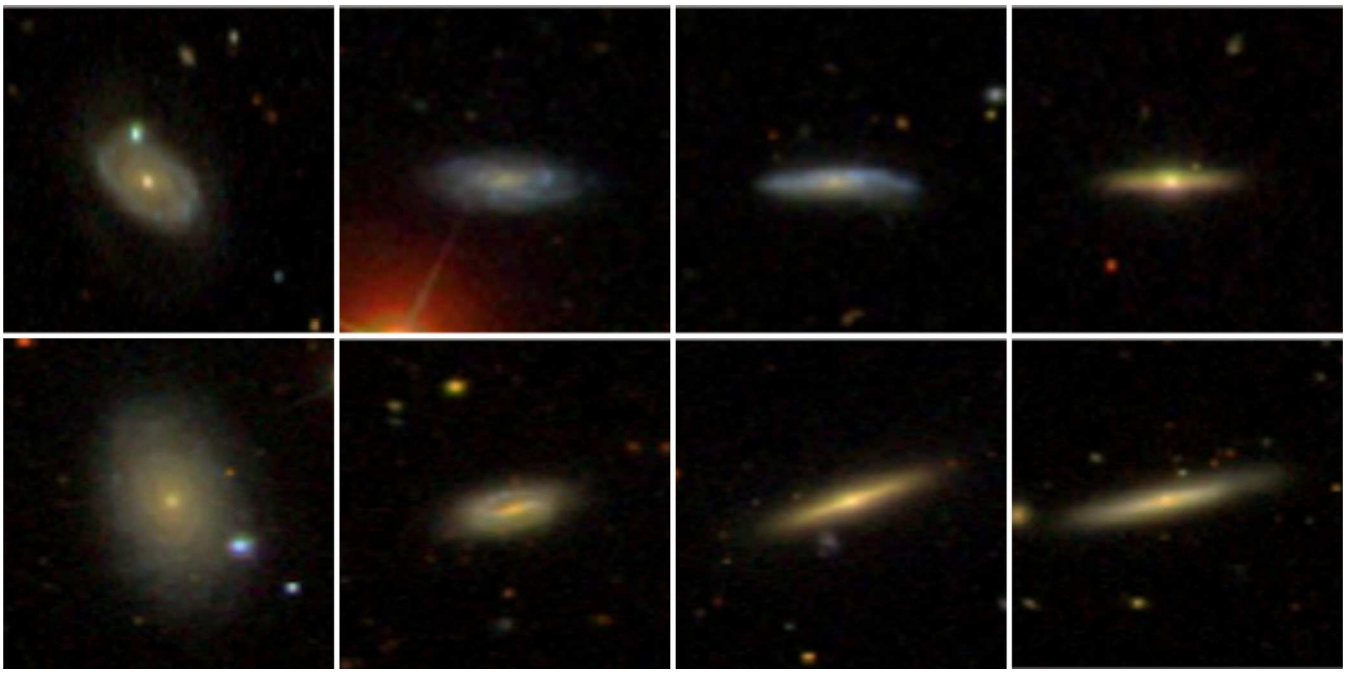

Figure 8. SDSS images of eight galaxies that are classified as early in the GOLDMINE data base; however, Galaxy Zoo gives them a greater than 80 per cent likelihood of being a late-type. The upper row is classified as E, and the lower is classified as S0. The galaxies are sorted left to right with galaxies on the right being closer to edge-on.

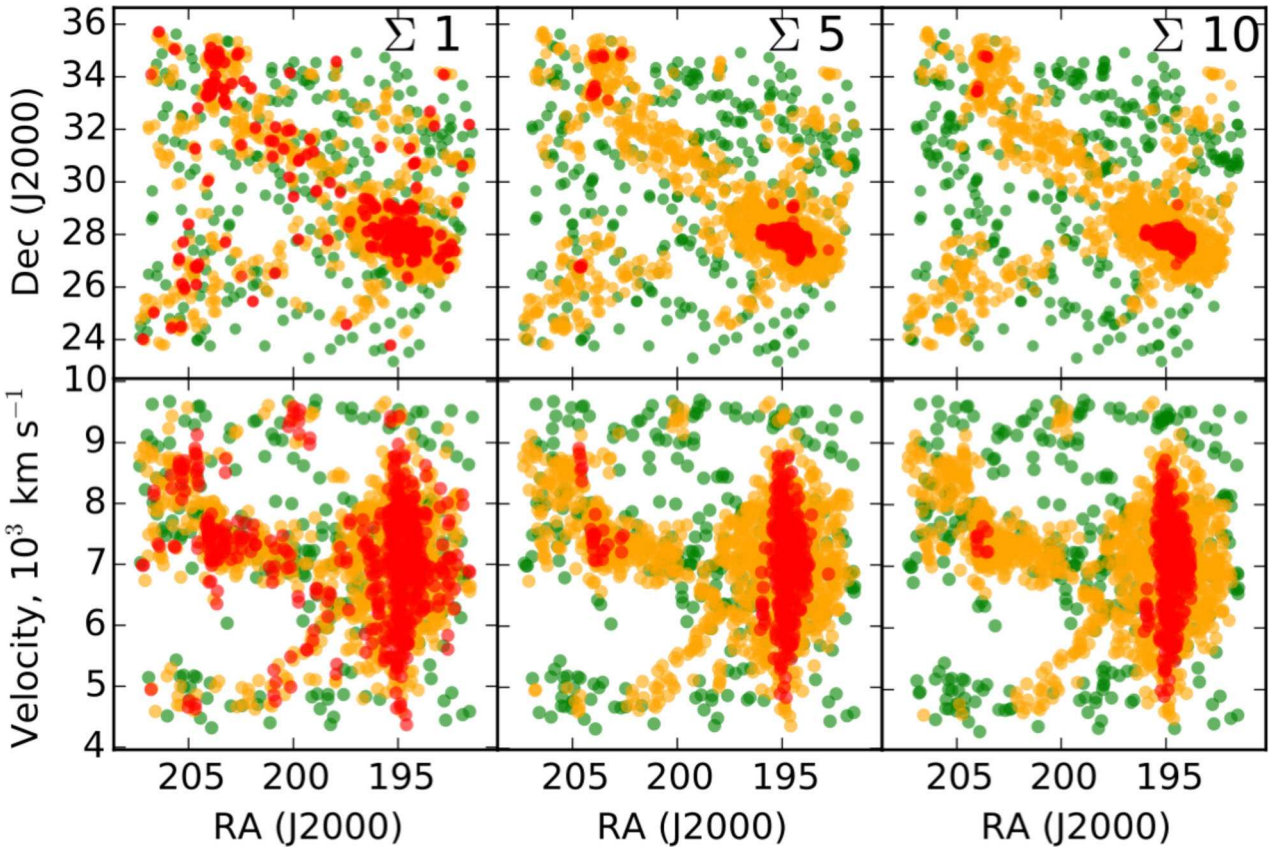

Figure 9. The above illustrates the changing values of Σ_N for the 1st, 5th and 10th nearest neighbours in our sample (left to right). The upper three plots are spatial plots in RA and Dec.; the lower three are for velocity and RA. Each point has been colour coded with green ($\Sigma_N < 1$ Mpc^{-2}), amber ($1 < \Sigma_N < 20$ Mpc^{-2}) and red ($20 < \Sigma_N$ Mpc^{-2}) to indicate low, medium and higher density regions.

we have drawn our sample from a greater area than the NGP *Herschel* field, but with our original velocity selection for the cluster and filament.

Fig. 9 illustrates the merit of each Σ_N statistic and what scale of environment it traces. Σ_{10} effectively smooths over the largest spatial scale and is sensitive to the larger scale structures. Conversely, Σ_1 and Σ_5 are sensitive to a galaxy's more immediate environment. As expected, all Σ_N statistics are highest in the cluster core. However, Fig. 9 shows that within the filament there are a number of higher density regions that can probably be associated with small groups of galaxies.

5 FIR RESULTS

5.1 Detection rates

Our Coma and filament FIR data are obtained from the positions of optically selected galaxies in the CCC/CFC. This is not ideal as we would prefer for our analysis to select galaxies via their FIR flux density. The problem of course is identifying which FIR sources belong to the cluster and which are in the background. Fig. 10 shows the distribution of optical magnitudes in the SDSS *r* band for all CCC/CFC (black) galaxies compared to just those detected at 250 μm in the *Herschel* data (cyan). We do not detect any galaxies in the FIR fainter than $r = 17.5$, which is below the limit of our optical selection. So, from this our expectation is that a deeper optical catalogue would not significantly increase the numbers of FIR detections in our current data. However, there is still of course the possibility of sources with unusual ratios of optical to FIR emission that are detected in the cluster/filament by *Herschel*, but are too faint to appear in the optical catalogue.

This is an issue we have investigated before for the Virgo (Davies et al. 2012) and Fornax clusters (Fuller et al. 2014). Our conclusion was that there is no evidence for a significant population of FIR sources missed by our optical selection. We have carried out a similar analysis here and come to the same conclusion. Our method is fully described in Davies et al. (2012), but briefly we compare the 250 μm number counts in an area away from the cluster with those over the cluster region, in this case within the virial radius (see Fig. 11). Although we are dealing with large numbers in the background compared to those in the cluster, we find no evidence for an excess population in the cluster field. The black line in Fig. 11 shows the counts for an eastern quadrant of the NGP field where contamination by foreground (filament) galaxies is at its lowest (Fig. 3) – these are the 'background' counts. The red line shows the counts from within the cluster virial radius; these counts only exceed the 'background' at bright flux densities due to the bright cluster sources. The counts of objects detected using our optical selection are shown in blue. There is no evidence, within the errors, for a large population of faint cluster FIR sources that are missed by having an optical rather than an FIR selection criteria, i.e. the red line only exceeds the black line at bright flux densities.

With the above caveat on optical selection, Table 4 shows how many galaxies were detected above a 3σ noise level in each band in the *Herschel* data. The SPIRE 250 μm band has the highest detection rate, something that has previously been noted by Auld et al. (2013)

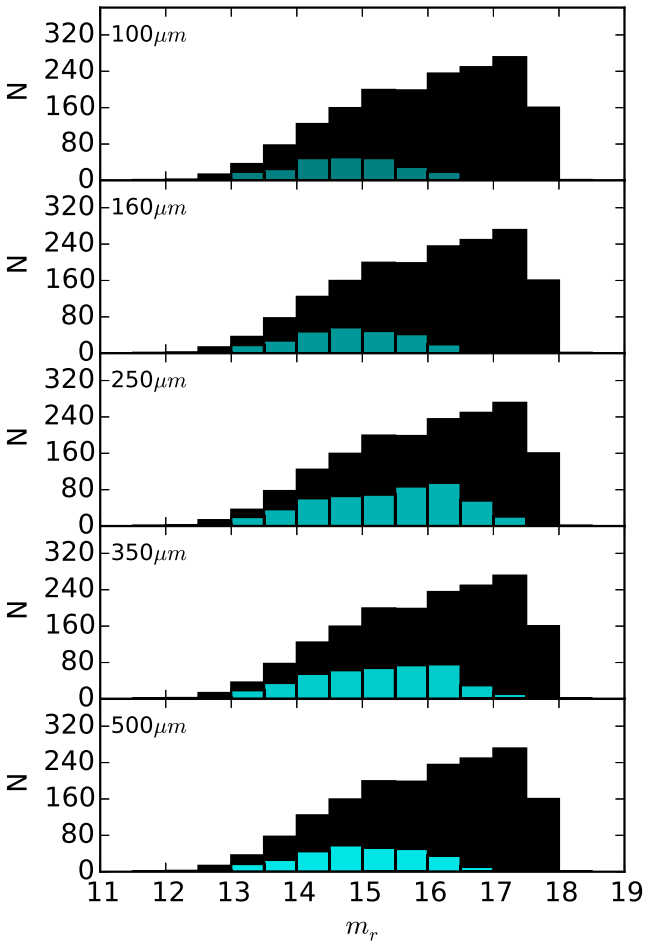

Figure 10. A histogram of r-band optical magnitude (m_r) for the CCC/CFC galaxies – the black and cyan bars are the total (optical) and FIR (250 μm) detected galaxies, respectively.

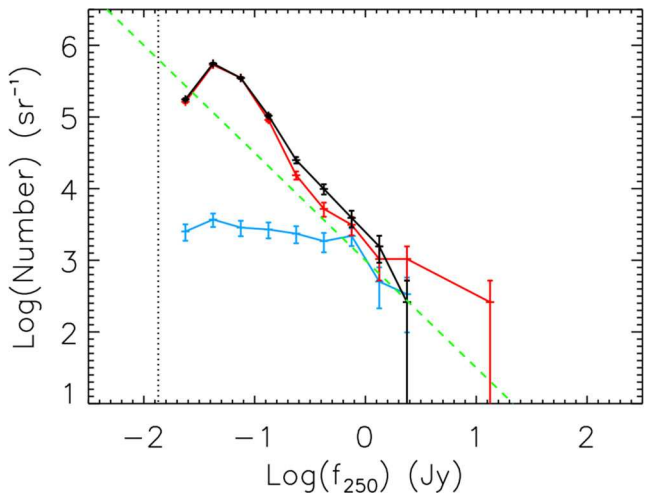

Figure 11. The 250 μm flux density of galaxies against number per steradian. The black line is for an eastern quadrant of the NGP field, where contamination by foreground galaxies is at its lowest (Fig. 3), while the red line is for the NGP within the virial radius of the cluster. The blue line is for CCC galaxies detected at 250 μm. The green dashed line has a slope of 1.5 and indicates the expected counts for a non-evolving Euclidean universe. The black dotted line indicates the minimum flux density detectable in the NGP field.

and Fuller et al. (2014) in Virgo and Fornax, respectively. This is due to a combination of instrument sensitivity and the typical shape of a galaxy's SED. Consequently, we will use the 250 μm band observations extensively in the below analysis and discussion. At 250 μm we detect 99 of 774 (13 per cent) of galaxies in the cluster and 422 of 951 (44 per cent) of galaxies in the filament – a significant difference and of course primarily due to the very different morphological mix (Table 3).

In order to better understand the properties of the galaxies we detect, we can estimate the limiting dust mass required for a detection at 250 μm. The lowest detected 250 μm flux in our FIR catalogue is ∼15 mJy. Assuming a dust temperature of 20 K (see below), the corresponding limiting dust mass is $\log_{10}(M_{\rm dust}/{\rm M}_\odot) = 6.1$. If we assume that a typical late-type galaxy has a dust-to-stellar mass ratio of $\log_{10}(M_{\rm dust}/M_{\rm stars}) = -3$ (Cortese 2012), then we should detect all galaxies with stellar masses of $\log_{10}(M_{\rm stars}/{\rm M}_\odot) > 9.1$. According to Brinchmann et al. (2004), the stellar mass limit for a galaxy with the mass-to-light ratio appropriate for a 13.6-Gyr-old stellar population with an apparent magnitude of $r = 17.8$ (the magnitude limit) and at the distance of Coma is also $\log_{10}(M_{\rm stars}/{\rm M}_\odot) \approx 9.0$.

Table 5 shows the detection rate for each morphological type (as defined above using Galaxy Zoo) within both the cluster and filament. As expected, late-type galaxies have the highest detection rate in both cluster and filament (of the order of 50 per cent). Conversely, early-type galaxies have the lowest detection rate (of the order of 10 per cent). Both early- and late-type detection rates are statically identical between the two samples, whereas uncertain-type galaxies have far lower detection rates inside the cluster environment (9 and 35 per cent for the cluster and filament, respectively). Far fewer morphologically uncertain (S0/Sa?) galaxies are detected in the FIR in the cluster compared to the field, suggesting that their star formation has been switched off in the cluster, but that their morphology has been unaffected.

For each morphological type, we have compared the positions and velocities of the FIR detected and undetected galaxies (Fig. 12). The black and coloured markers in the left-hand panels indicate the spatial position of each galaxy. The dashed black circle in the left-hand panel marks the virial radius of the cluster. The right-hand panels show histograms of radial velocity. For each histogram of velocity, we have fitted a Gaussian using χ^2 minimization, where errors are $\sqrt{N}$ galaxies per bin; the purple and grey histograms represent fits to the detected and undetected galaxies, respectively. We have listed the average projected cluster radius for detected and undetected galaxies in the cluster as well as the derived velocity dispersions in Table 6.

All three morphological types have velocity dispersions that are statistically identical for FIR detected and undetected galaxies. All the velocity dispersions are also statically identical to the overall velocity dispersion (∼ 900 km s^{-1}) of the cluster. If any of the morphological populations had a velocity dispersion that was greater than that of the cluster as a whole, it would imply that it was less relaxed and thus probably far later in joining the cluster. The fact that all our morphological types show no evidence of a different velocity dispersion implies that they have been in the cluster longer than a crossing time of a few Gyr. This is longer than the gas stripping time-scale even for the most massive galaxies (Boselli & Gavazzi 2006).

With regard to position in the cluster, as expected late-type galaxies have the largest average projected cluster radius ($0.55R_{\rm virial}$). Conversely, early-type galaxies have the smallest average projected cluster radius ($0.37R_{\rm virial}$). Both late- and early-type galaxies show

Table 4. The detection rates for each *Herschel* band in the cluster and the filament. In total, there are 744 and 951 optically detected galaxies in the cluster and filament, respectively.

Band	Cluster		Filament	
(μm)	Number of detections (N)	Detection rate (per cent)	Number of detections (N)	Detection rate (per cent)
100	60	8	187	20
160	55	7	210	22
250	99	13	422	44
350	80	10	355	37
500	54	7	247	26

Table 5. Detection rates for each morphological type in the cluster and filament.

Morphological type	Cluster $N \pm \sqrt{N}$	Filament $N \pm \sqrt{N}$
Late	37 ± 6	239 ± 16
Uncertain	47 ± 7	164 ± 13
Early	15 ± 4	19 ± 4

no difference in mean radius between FIR detected and undetected galaxies ($<2\sigma$). Uncertain-type galaxies are the only sample that shows any significant difference in spatial position when selected by their FIR properties (0.4 and $0.6R_{\rm virial}$ for detected and undetected galaxies, respectively). This is somewhat counterintuitive, with the detected galaxies having an average spatial position closer to the cluster centre than those not detected.

5.2 Analysis of SED fits, dust masses and temperatures

There are 521 CCC/CFC galaxies detected in the FIR at 250 μm, but not all of these are detected in all five *Herschel* bands. For the 198 galaxies detected in all five bands, we have fitted their SEDs with single-temperature modified blackbody curves using $\beta = 2$. The average χ^2 goodness-of-fit value for the entire sample is $\langle \chi^2_{\rm dof=3} \rangle = 2.7$ (where $\chi^2_{\rm dof=3} < 7.8$ corresponds with a confidence level of 95 per cent) indicating that for the majority of the sample the SEDs are well fitted. Seven galaxies have $\chi^2_{\rm dof=3} > 7.8$ indicating that a single temperature component may not be sufficient to model their FIR emission. In Appendix C, we show the SEDs and modified blackbody fits for each galaxy. Histograms of dust mass, dust-to-stellar mass and dust temperatures produced from the SED fitting process are shown in Fig. 13.

Fig. 13 shows that detected late-type galaxies have dust masses ranging from $\log_{10}(M_{\rm dust}/{\rm M}_\odot) = 7.0$ to 8.3 and temperatures of 16.0–25.5 K, with mean values of $\log_{10}(M_{\rm dust}/{\rm M}_\odot) = 7.63 \pm 0.02$ and 20.0 ± 0.1 K. Uncertain-type galaxies have dust masses ranging from $\log_{10}(M_{\rm dust}/{\rm M}_\odot) = 6.7$ to 8.3 and temperatures of 16.2–28.7 K, with mean values of $\log_{10}(M_{\rm dust}/{\rm M}_\odot) = 7.33 \pm 0.04$ and 21.7 ± 0.5 K. Early-types have a narrower range of dust masses of $\log_{10}(M_{\rm dust}/{\rm M}_\odot) = 6.9$ to 7.5 and temperatures of 16.2–26.0 K, with mean values of $\log_{10}(M_{\rm dust}/{\rm M}_\odot) = 7.3 \pm 0.04$ and 21.0 ± 0.2 K. This observed warmer dust temperature for early-type galaxies has previously been observed in both the Virgo (Davies et al. 2014) and Fornax (Fuller et al. 2014) clusters and may be due to additional heating by hot X-ray gas.

CCC/CFC galaxies have mean dust-to-stellar mass ratios of $\log_{10}(M_{\rm dust}/M_{\rm stars}) = -3.6 \pm 0.04$, -2.93 ± 0.01 and -2.75 ± 0.01 for early-, uncertain- and late-types, respectively. As expected from our previous results for Virgo and Fornax (Auld et al. 2013; Fuller et al. 2014), late-types have richer and cooler dust reservoirs, and early-types have a relatively depleted and warmer ISM.

In Table 7, we use the Kolmogorov–Smirnov (K-S) two-sample test to make a more quantitative comparison between the cluster and filament's early-, uncertain- and late-type galaxy populations with respect to dust mass, dust-to-stars ratio and dust temperature. The K-S test shows that for a given morphological type, the FIR properties of galaxies in the cluster and filament are statistically very similar with the one obvious exception of early-type galaxy dust temperatures; early-types have hotter dust temperatures in the cluster environment. Just why this occurs is not clear, though it is possible it has something to do with the cluster X-ray gas. The above results suggest, however, that on the whole the different environments have had very little effect on the dust properties of their constituent galaxies.

We have also used (Table 7) H I-deficiency values calculated for 70 galaxies from Gavazzi et al. (2006) to compare galaxies that are H I-normal (H I-def. ≥ 0.5) with H I-deficient (H I-def. < 0.5) – these galaxies are exclusively late-type. A K-S test shows that H I-normal and H I-deficient galaxies are statically identical with respect to dust mass and temperature. However, with respect to dust-to-stellar mass ratio, H I-normal and H I-deficient galaxies are unlikely to be drawn from the same distribution. Galaxies that are depleted in H I are also depleted in dust (Cortese 2012). Gavazzi et al. (2006) have previously showed that H I-deficiency decreases with cluster centric distance with the most H I-deficient galaxies at the cluster centre. The implication is that H I-deficiency traces those galaxies most strongly affected by the ram pressure stripping of gas within the cluster environment. The above result – that galaxies have different dust-to-stellar mass ratios when separated by H I-deficiency – shows that this physical process can affect both the atomic gas and dust properties of typical late-type galaxies. This result is not new having been shown previously by Cortese et al. (2010) – they showed that the radial extent of dust was truncated for H I-deficient galaxies.

5.3 Chemical evolution

Given that we have for a sub-sample of our galaxies measures of the mass of gas (atomic) and metals (both in dust and the gas phase), we can consider and compare the chemical evolution of cluster and filament galaxies. We have 80 filament and 18 cluster galaxies for which both H I and gas phase metallicity values are available.

Edmunds (1990) shows that a galaxy's metallicity $Z_{\rm Total} = M_{\rm metals}/M_{\rm gas}$ is related to the gas fraction ($f = M_{\rm gas}/(M_{\rm stars} + M_{\rm metals} + M_{\rm gas})$) in the following way $Z_{\rm Total} \leq p \ln(1/f)$, where the equality applies to the closed box model, i.e. one in which there are no additional inflows or outflows of gas after the galaxy has

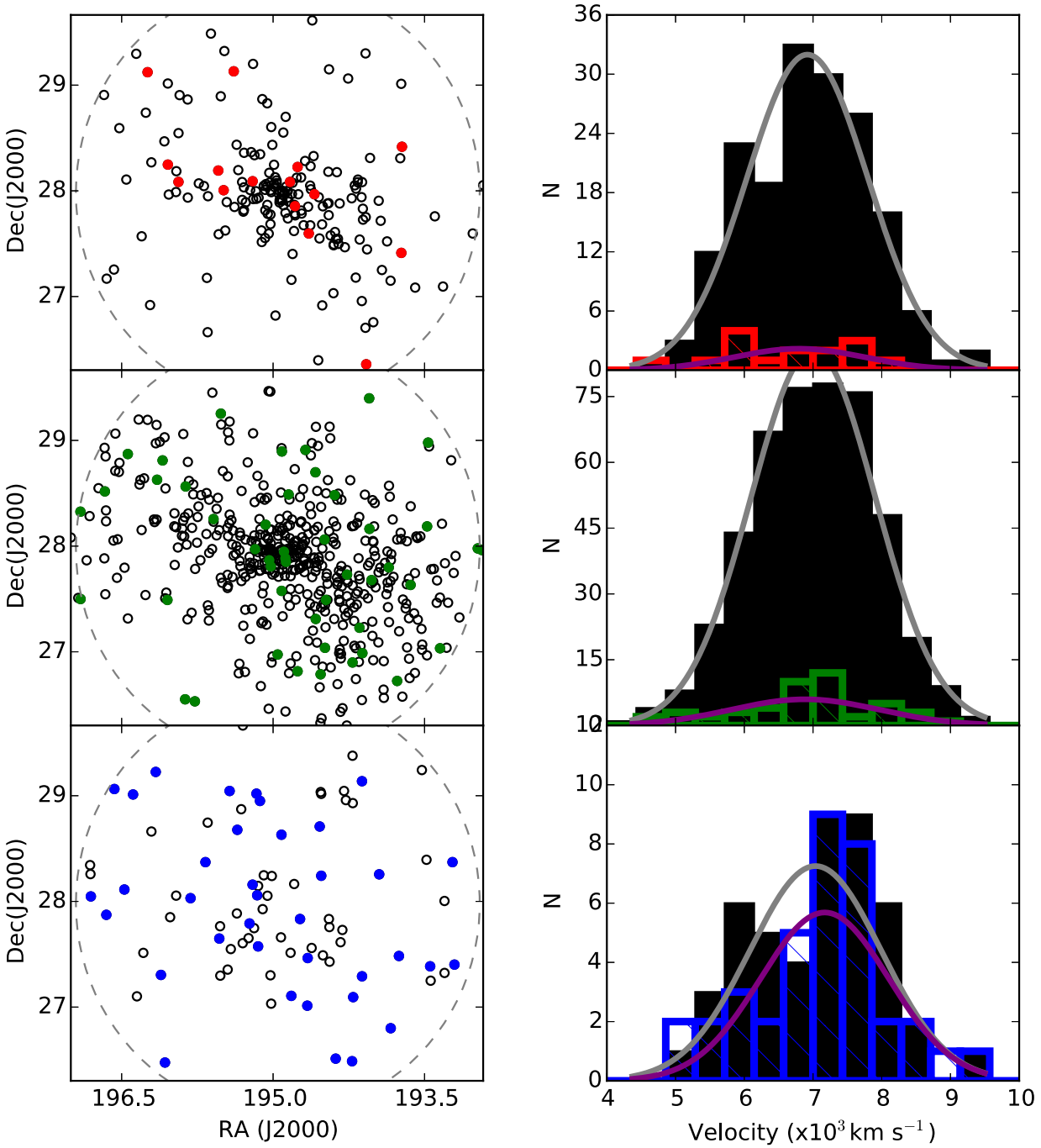

Figure 12. The locations and velocities of galaxies within the virial radius of the cluster. Coloured and black markers and histograms designate FIR detected and undetected galaxies, respectively. The three morphological types are shown from top to bottom in red, green and blue representing early-, uncertain- and late-type galaxies. The left-hand panels show their location in RA and Dec. The right-hand panels show histograms of radial velocity – the purple and grey lines are Gaussian fits to the histograms of detected and undetected galaxies, respectively.

Table 6. This table contains information relating to Fig. 12 for the cluster sample. The radius refers to the average projected cluster centric radius for either FIR detected or undetected galaxies of a given morphological type. The velocity dispersions have been obtained by fitting a Gaussian function to the velocity histograms.

Morphological type	Radius ($R/R_{\rm virial}$)		Difference	Velocity dispersion (km s^{-1})		Difference
	Detected	Undetected		Detected	Undetected	
Late	0.48 ± 0.04	0.59 ± 0.04	1.9σ	935 ± 154 (0.5)	956 ± 117 (0.56)	0.1σ
Uncertain	0.42 ± 0.01	0.57 ± 0.04	3.6σ	1070 ± 206 (0.9)	906 ± 20 (0.37)	0.8σ
Early	0.43 ± 0.07	0.36 ± 0.02	1.0σ	951 ± 206 (0.29)	884 ± 46 (0.67)	0.3σ

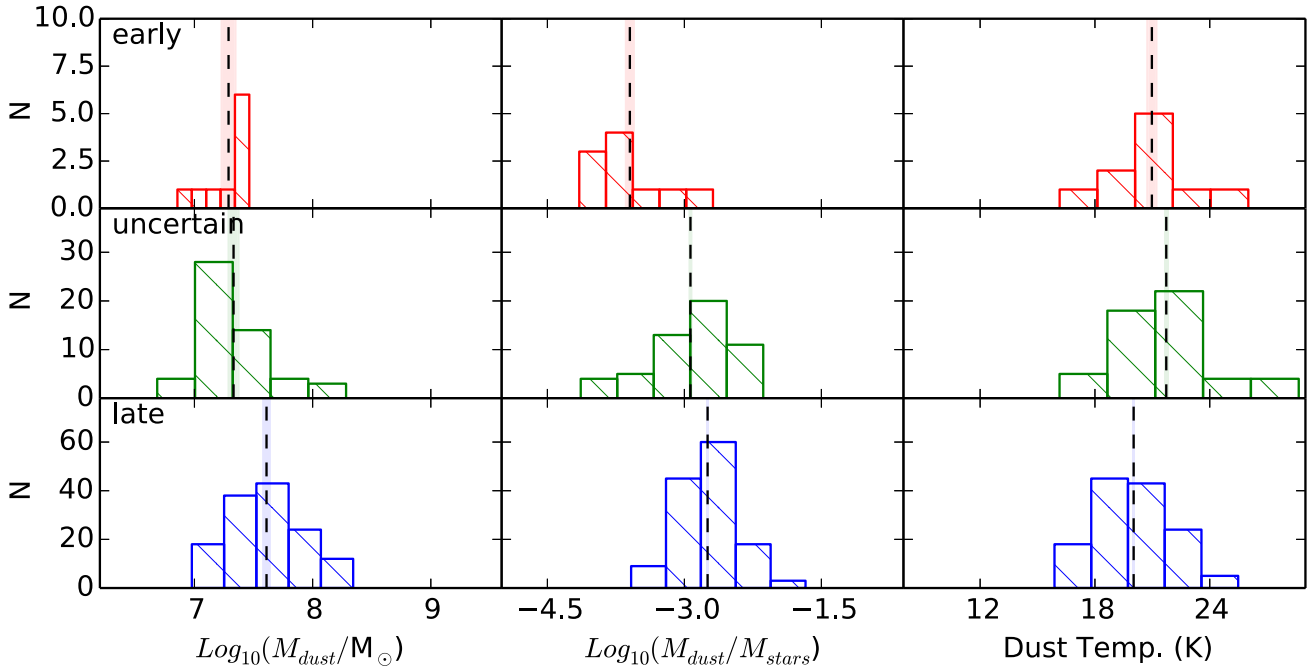

Figure 13. Histograms of dust mass (left), dust-to-stellar mass (centre) and dust temperature (right) for 198 galaxies detected in all five *Herschel* bands and fitted with a modified blackbody. Early-, uncertain- and late-type galaxies are plotted in red, green and blue, respectively. The vertical dashed line indicates the mean of each sample.

Table 7. A statistical comparison of the cluster (Sample 1) and filament (Sample 2) plus a comparison with normal and H I-deficient galaxies. μ is the mean value and σ the associated error. The K-S test compares the distribution of values in each sample. The D-value is the absolute maximum distance between the cumulative distributions of the two samples and the null hypothesis (that the two samples were drawn from the same distribution) is rejected if the p_{value} is less than our acceptable significance level.

Sample 1	Sample 2	$\mu_1(\sigma_1)$	$\mu_2(\sigma_2)$	K-S test	
				D-value	p_{value}
Dust mass ($\log(M_{\mathrm{Dust}}/\mathrm{M}_{\odot})$)					
Cluster early	Filament early	7.25(0.09)	7.35(0.05)	0.333	0.89
Cluster uncertain	Filament uncertain	7.33(0.07)	7.33(0.05)	0.14	0.974
Cluster late	Filament late	7.66(0.06)	7.6(0.03)	0.12	0.914
H I-normal	H I-deficient	7.64(0.06)	7.72(0.05)	0.317	0.5
Stellar mass/dust mass ($\log(M_{\mathrm{dust}}/M_{\mathrm{stellar}})$)					
Cluster early	Filament early	− 3.74(0.14)	− 3.39(0.23)	0.583	0.254
Cluster uncertain	Filament uncertain	− 3.05(0.14)	− 2.89(0.07)	0.168	0.892
Cluster late	Filament late	− 2.78(0.06)	− 2.74(0.03)	0.144	0.762
H I-normal	H I-deficient	− 2.98(0.11)	− 2.65(0.04)	0.544	0.036
Dust temp. (K)					
Cluster early	Filament early	22.12(0.77)	19.25(0.9)	0.833	0.03
Cluster uncertain	Filament uncertain	21.51(0.49)	21.81(0.43)	0.179	0.845
Cluster late	Filament late	20.66(0.44)	19.88(0.18)	0.229	0.205
H I-normal	H I-deficient	20.46(0.99)	20.37(0.32)	0.213	0.918

formed. p is the stellar yield, which is the fractional mass of metals per unit mass of gas freshly formed in nucleosynthesis. Edmunds (1990) defines the effective yield as $p_{\mathrm{eff}} = \frac{Z_{\mathrm{Total}}}{\ln(1/f)}$, i.e. the derived yield regardless of inflow or outflow. Essentially p depends on physical processes in the interior of stars and the stellar IMF, while p_{eff} has an additional dependence on the inflow or outflow of gas either pristine or metal enriched (Davies et al. 2014). We can see if cluster galaxies have a different value of p_{eff} to filament galaxies so indicating that their star-forming history has been affected by the cluster environment.

In order to calculate the total gas mass of each galaxy, we must take account of all the other major gas phases: molecular hydrogen, helium and the gas in the warm and hot components. Davies et al. (2014) estimate that $M_{\mathrm{Gas}}^{\mathrm{Total}} = 2.5 M_{\mathrm{H\,I}}$ for galaxies in the Virgo cluster. This is derived from the measured H I mass, the mean ratio of molecular to atomic gas, the abundance of helium and the gas in the warm and hot components. We use this relation to adjust our H I masses to take account of all phases of the gaseous ISM.

Again following Davies et al. (2014), we estimate the total mass in metals to be $M_{\mathrm{Metals}} = 1.2 Z_{\mathrm{Gas}} M_{\mathrm{H\,I}} + M_{\mathrm{Dust}}$. Z_{Gas} is

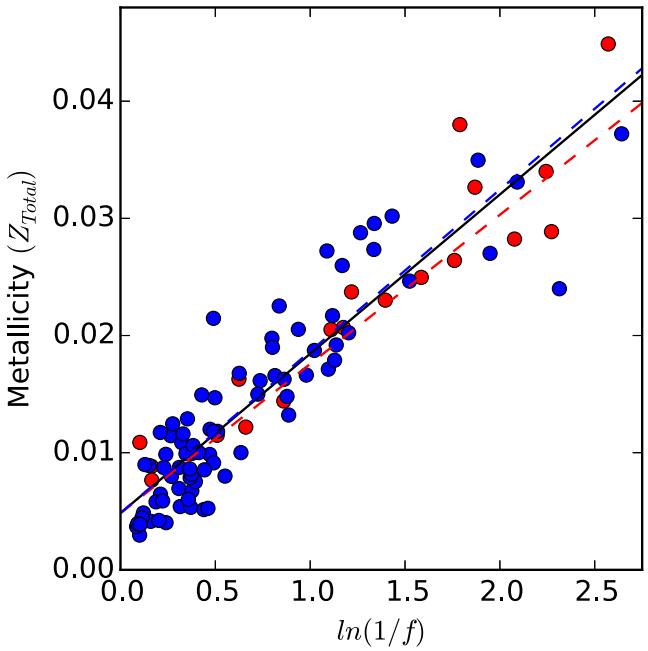

Figure 14. The derived metallicity (taking account of both metals in dust and the gaseous phases) against $\ln(1/f)$, where f is the gas fraction. Red and blue markers are used for cluster and filament galaxies, with red, blue and black lines being lines fitted to the cluster, filament and overall samples, respectively. The gradients of these lines are equal to the effective yield $p_{\rm eff}$.

derived from the oxygen abundance ($12.0 + \log_{10}(\mathrm{O/H})_{\odot}$). Asplund & García Pérez (2001) give the solar oxygen abundance as $12.0 + \log_{10}(\mathrm{O/H})_{\odot} = 8.69$ and $Z_{\odot} = 0.014$; this allows us to convert oxygen abundance (O/H) to total metallicity in the gas phase ($Z_{\rm gas}$) using the relation $Z_{\rm gas} = 29.2(\mathrm{O/H})$, and this assumes solar abundance ratios. However, this does not account for the metals in the warm and hot phases of the ISM. Davies et al. (2014) use the work of Gupta et al. (2012) and estimate that the mass of metals in the hot and warm phases of the ISM to be $0.2 Z_{\rm gas} M_{\rm H\,I}$, giving $M_{\rm Metals} = 1.2 z_{\rm gas} M_{\rm H\,I} + M_{\rm Dust}$. The 'total' metallicity ($Z_{\rm Total}$) is then calculated from both the gaseous and dusty ISM, defined as $Z_{\rm Total} = M_{\rm Metals}/M_{\rm Gas}^{\rm Total}$.

As an aside, we find that the mean mass fraction of metals in the dust is 0.4 ± 0.1, which agrees with previous estimates of 0.5 by Meyer, Jura & Cardelli (1998) and Whittet (1992). Davies et al. (2014) performed the same analysis for galaxies in the Virgo cluster and found a value of 0.50 ± 0.02.

In Fig. 14, we plot the total metallicity ($Z_{\rm Total}$) against the logarithm of the reciprocal of the gas fraction ($\ln(1/f)$). The red and blue markers and lines represent cluster and filament galaxies, respectively. We fit a linear relation with a y-axis intercept of 0; the gradient of this line is the effective yield ($p_{\rm eff}$). The effective yields of the cluster and filament are 0.017 ± 0.01 and 0.019 ± 0.01, respectively. Thus, the two are statically identical. The black line is a fit to all the galaxies and gives an effective yield of 0.018 ± 0.01. The galaxies appear well fitted by a linear relation. In terms of a chemical evolution model, galaxies in the cluster appear identical to galaxies in the filament – there is no evidence that cluster galaxies, for example, have been stripped of gas and so 'locking in' a fixed metallicity at a low gas fraction.

6 TRENDS WITH DENSITY

In this section, we will consider how dust-to-stars[9] and gas-to-stars ratios, sSFR,[10] stellar mass and morphological mix depend on local galaxy density (Σ_1, Σ_5, Σ_{10} and projected cluster radius). We will also make use of the Galaxy Zoo morphological classifications in a slightly different way. Using the probability weightings described earlier (p(S) for a spiral and p(E) for an elliptical), we now define a new parameter (Φ), where $\Phi = p(\mathrm{S}) - p(\mathrm{E})$. This is a new non-integer way of describing a galaxy's morphology, where values of $\Phi \simeq 1$ and -1 are expected for a definite late- (spiral) and early-type galaxy. As part of our trends with density analysis, we will now define early-type galaxies as those with negative Φ and late-types as those with positive Φ. Our results are summarized in Fig. 15.

For each parameter in Fig. 15, we have used evenly spaced bins over the logarithmic density range for each morphological type (early and late). Each point is the mean value in the bin with the circle size purely a relative measure of the number of galaxies in each bin. The error bar is the standard deviation in the bin divided by the square root of the number of galaxies in that bin. If a bin has less than three galaxies in it, it is discounted and neither plotted or fitted. For each morphological type, parameter versus density plot, we have fitted a straight line (e.g. $y = mx + C$), using a χ^2 minimization. We test whether or not each fit is consistent with a change with density (i.e. $m \neq 0$).

For each parameter and morphological type, we have calculated from Fig. 15 the number of density tracers that are consistent with a change with density ($m \neq 0$ with a significance greater than 3σ). If all four density tracers are consistent with a change with density, then it is designated as having a 'Strong' change. If two or three density tracers are consistent with a change with density, then it is designated as having a 'Moderate' change. If only one density tracer is consistent with a change with density, then it is designated as having a 'Weak' change. Finally, if no density tracers are consistent with a change with density, then it is designated as having 'No' change. Clearly, the different measures of density should apply over different spatial scales, but as is clear from Fig. 15 trends in the data are apparent independent of the density scale used. Table 8 lists each parameter and how strong (if at all) any change with density is. The bottom line is that there is pretty good evidence that late-type galaxies do change their properties dependent on the local environment, but that early-type galaxies do not.

Clearly, the gas-to-stars ratio of late-type galaxies is strongly affected by the local density (Fig. 15). This is consistent with the idea, discussed above, that gas is stripped from galaxies as they move through the cluster environment. Those galaxies residing in the highest density environments and/or at the smallest projected radii from the cluster centre being most affected by the gas loss. Alternately, rather than gas loss the gas may have been more efficiently converted into stars. Fig. 15 also clearly shows that stellar mass is increasing with environmental density actually supporting the second alternative that gas has been taken up into stars at a faster rate in the denser cluster environments.

[9] For galaxies that are detected at 250 μm, but could not be fitted with an SED because they had too few other data points, we have estimated their dust mass using the 250 μm flux density and a fixed dust temperature of 20 K. This lets us add a further 323 galaxies to our sample, yielding a total sample of 521 galaxies with dust masses in both the filament and cluster.
[10] sSFR is the specific star formation rate, which is just the SFR divided by stellar mass.

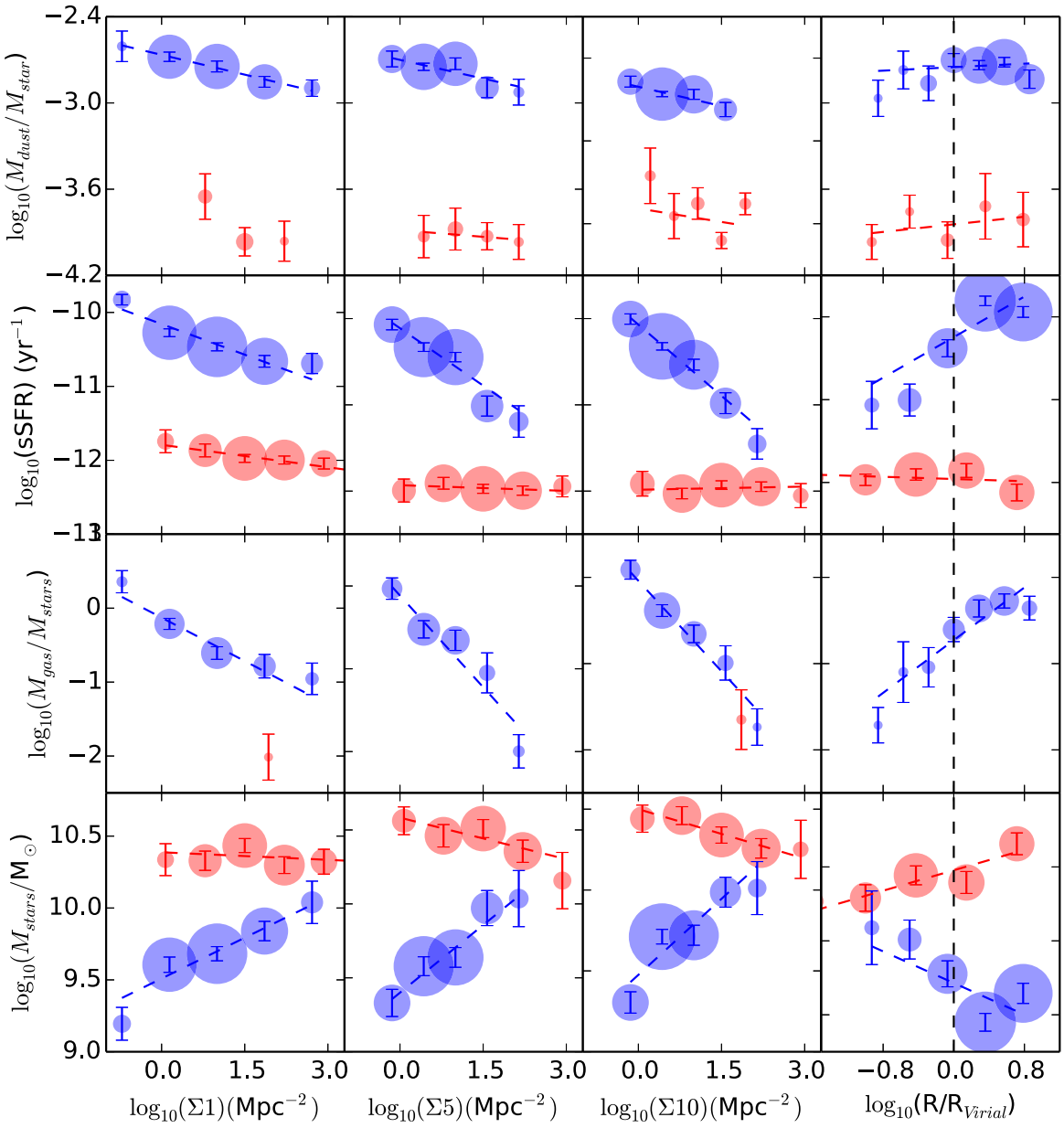

Figure 15. Illustration of how four different galaxy parameters change with local galaxy density as traced by Σ_1, Σ_5, Σ_{10} and with projected cluster radius. Red and blue markers and lines are for early- and late-type galaxies, respectively. Each point indicates a given density bin's mean value, and its size represents the relative number of galaxies in each bin. Each line is fitted using a χ^2 minimization technique.

Table 8. For each morphological type and parameter, we measure how many density tracers are consistent with a change ($m \neq 0$) then $N = 4$, Strong; $N = 2$ or 3, Moderate; $N = 1$, Weak; and $N = 0$ is shown in parentheses.

	Late	Early
Dust-to-stars	Moderate (2)	No (0)
sSFR	Moderate (3)	Weak (1)
Gas-to-stars	Strong (4)	–
Stellar mass	Moderate (3)	Weak (1)

We can also investigate the morphology–density relation using our new measure of morphology Φ. In Fig. 16, we have calculated the change of Φ with all four environmental tracers. Φ is strongly affected by galaxy density even over the scales measured by Σ_1 – so if we have a near neighbour (10s to a 100 kpc away) of similar mass (we only have a small range of stellar masses in our sample, see Fig. 15) we are more likely to be of an earlier type. Interestingly, Φ is approximately equal to zero just about at the cluster virial radius.

7 MASS DISTRIBUTIONS

In order to understand how the baryonic components of galaxies change as a whole between the cluster and filament, we have created stars, gas and dust mass distributions (Fig. 17). To do this, we have had to make some assumptions. First, we have no information about the precise distance to individual galaxies so we assume that they are all, whether in the cluster or filament at the same distance as the cluster (105 Mpc). Secondly, ideally we would like to select by stellar mass to create the stellar mass function, atomic hydrogen

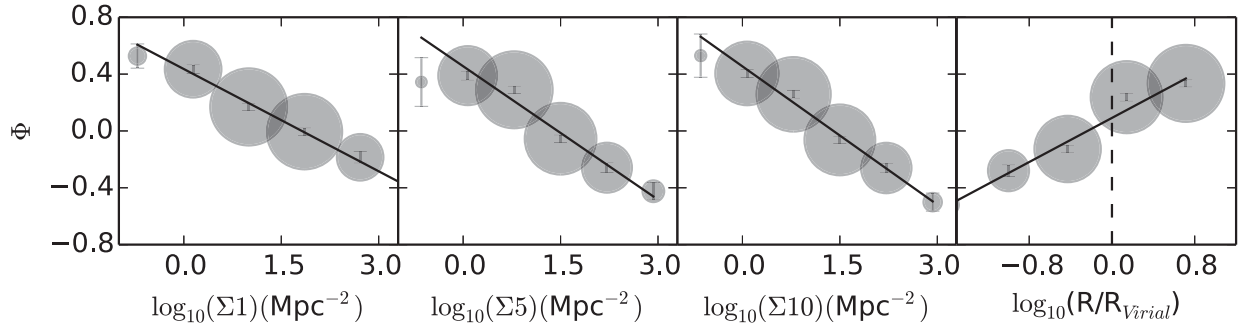

Figure 16. Morphology (Φ) as a function of galaxy density as traced using Σ_1, Σ_5, Σ_{10} and projected cluster radius (left to right). Each marker represents a given density bin's mean value, and its size represents the number of galaxies in each bin. Each line is fitted using a χ^2 minimization.

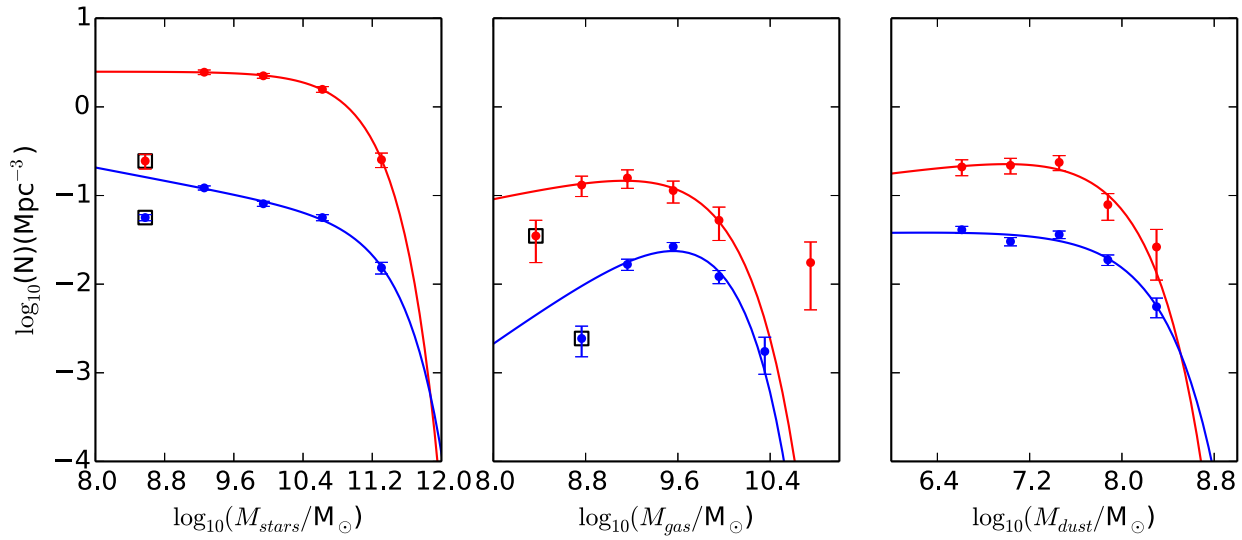

Figure 17. Mass distributions for galaxies in the cluster and filament. Left to right are the stellar, gas (atomic) and dust mass data. The red and blue markers and lines refer to the cluster and filament samples, respectively. The lines are Schechter function fits to the data. The points with black squares were excluded from the fitting process.

mass for the gas mass function and dust mass for the dust mass function. In reality, we have a complex selection of SDSS *r*-band magnitude of 17.8 for the stars, this plus a varied 21 cm detection limit for the gas and the SDSS plus *Herschel* limit for the dust – this is why we will refer to what we derive as mass distributions rather than mass functions. Thirdly, the volumes to use to get densities are rather difficult to determinate. With these provisos, we will concentrate on the bright end of the mass functions, where we might hope to have completeness and on the general shape of the mass distributions rather than their difficult to determine normalizations.[11]

To get some rough feel for the numbers involved, we estimated the volume of the cluster as a sphere with a virial radius of 3.1 Mpc and hence a volume of ∼125 Mpc^3. Estimating the volume of the filament is not so straightforward because it is not a virialized region, in the same sense as the cluster, and so does not have a well-defined size. To make a crude comparison, we have assumed that the filament is a sheet of depth 6 Mpc ($\sim 2 \times R_{\rm virial}^{\rm Coma}$) with a cross-sectional area the same as the area covered by the NGP field at a distance of 105 Mpc (23.4 × 21.7 Mpc). We then subtract the volume of the cluster from this region yielding a volume for the filament of 2873 Mpc^3.

We have fitted the below Schechter function (given in terms of linear rather than logarithmic units) to each of the data sets shown in Fig. 17:

$$N(M)\,{\rm d}M = \phi^* \left(\frac{M}{M^*}\right)^{\alpha} {\rm e}^{-\frac{M}{M^*}} \frac{{\rm d}M}{M^*} \tag{4}$$

and then using

$$\rho = \phi M^* \Gamma(\alpha + 2) \tag{5}$$

calculated the mass density of each component from the derived best-fitting function values, see Table 9.

The stellar mass shown in the left-hand panel of Fig. 17 is probably the best constrained of all three mass distributions as it is derived from the complete optical sample. As noted above, the best-fitting Schechter parameter ϕ is set arbitrarily by the choice of volume, but using our values the cluster is about 20 times more dense than the filament (Table 9). The data in Table 9 also indicate that Coma is some three times more dense than Virgo and that the filament is about 50 times more dense than the general field (see references given in the caption to Table 9). M^* and α the so-called 'characteristic mass' and 'faint-end slope' are both independent of volume and thus interesting to compare. However, the values of M^* and α

[11] To overcome this problem to some extent, we do not fit the lowest mass point for either stellar or gas mass distributions. For our dust mass data, we can be a little more confident. As stated above, our dust mass limit is $\log_{10}(M_{\rm dust}/{\rm M}_\odot) \approx 6.4$ and so we fit all data above this limit.

Table 9. The tabulated values of the Schechter function fits from Fig. 17. The fits for stellar, gas (atomic) and dust mass are shown. We have calculated the mass density for each fit (see the text) and listed it in the rightmost column. References are as follows: (1) this paper, (2) Davies et al. (2014), (3) Dunne et al. (2011), (4) Panter et al. (2007) and (5) Davies et al. (2011).

Sample	ϕ (Mpc^{-3} dex^{-1})	M^* (10^9 M$_\odot$)	α	ρ (10^9 M$_\odot$ Mpc^{-3})	Ref
Stellar mass					
Coma	2.5 ± 0.08	89 ± 30	−1.0 ± 0.1	220 ± 10	(1)
Filament	0.05 ± 0.01	175 ± 48	−1.2 ± 0.1	10.2 ± 3.6	(1)
Virgo	0.3 ± 0.1	192 ± 117	−1.2 ± 0.1	67 ± 47	(2)
Field	0.0002 ± 0.0001	100 ± 20	−1.2 ± 0.1	0.2 ± 0.05	(4)
Gas mass					
Coma	0.3 ± 0.2	4.8 ± 3.2	−0.7 ± 0.4	1.3 ± 1.2	(1)
Filament	0.06 ± 0.01	3.9 ± 1.5	−0.08 ± 0.5	0.22 ± 0.10	(1)
Virgo	0.6 ± 0.3	4.5 ± 1.6	−1.0 ± 0.2	2.7 ± 1.7	(2)
Field	0.009 ± 0.001	5.0 ± 0.1	−1.50 ± 0.05	0.08 ± 0.01	(5)
Dust mass					
Coma	0.4 ± 0.2	0.06 ± 0.03	−0.8 ± 0.2	0.02 ± 0.02	(1)
Filament	0.04 ± 0.02	0.1 ± 0.04	−1.0 ± 0.2	0.04 ± 0.02	(1)
Virgo	0.7 ± 0.1	0.06 ± 0.01	−0.9 ± 0.1	0.04 ± 0.01	(2)
Field	0.006 ± 0.001	0.040 ± 0.004	−1.0 ± 0.2	0.0002 ± 0.0001	(3)

Table 10. The ratios of mass density (from Table 9) within each environment. We have normalized each ratio to stellar mass density.

Sample	$\log_{10}(\rho_{\rm gas}/\rho_{\rm stars})$	$\log_{10}(\rho_{\rm dust}/\rho_{\rm stars})$
Coma	$-2.2\,^{+0.3}_{-1.3}$	$-4.0\,^{+0.2}_{-0.5}$
Filament	$-1.7\,^{+0.2}_{-0.4}$	$-3.4\,^{+0.2}_{-0.6}$
Virgo	$-1.4\,^{+0.3}_{-1.2}$	$-3.2\,^{+0.2}_{-0.6}$
Field	$-0.5\,^{+0.1}_{-0.1}$	$-3.0\,^{+0.1}_{-0.2}$

Table 11. Mass parameters for the Coma cluster derived from optically selected galaxies.

Component	Mass (M$_\odot$)
Total stellar mass	2.8×10^{13}
Total gas mass	1.6×10^{11}
Total dust mass	2.5×10^{9}
Total baryonic (excluding X-ray gas)	2.8×10^{13}
Virial mass	2.9×10^{15}

for the cluster and filament samples are consistent ($<1\sigma$) with each other and with Virgo and the general field. From these data, there is no evidence that the environment has had any influence on the relative numbers of galaxies with different stellar masses.

The atomic mass distributions are shown in the central panel of Fig. 17. This is the poorest constrained of the three mass distributions as it represents the smallest fraction of the optical sample (58 and 172 galaxies in the cluster and filament, respectively). Again, with the provisos on volumes, Coma is about six times more dense in atomic gas than the filament – compared to the stars the gas is depleted in Coma. Most notable is the steepness of the field galaxy atomic gas mass distribution compared to Coma, filament and Virgo. The values of M^* and α for the cluster and filament samples are consistent ($<1\sigma$) with each other, but the fitting errors are large because of the small numbers.

The dust mass distribution is shown in the rightmost panel of Fig. 17 and is reasonably well constrained as it represents a significant fraction of the optical sample (88 and 379 galaxies in the cluster and filament, respectively). Most notable is the large gas-to-dust ratio of the filament. Again, the values of M^* and α for the cluster and filament samples are consistent ($<1\sigma$) with each other and with Virgo and the field.

We can take the mass densities (ρ) from Table 9 and create ratios that are usefully independent of the volume used. We have created one for each of the four environments (Coma, filament, Virgo and the field), see Table 10.

The Coma, filament and Virgo environments are all statically the same (Table 10) in terms of $\log_{10}(\rho_{\rm gas}/\rho_{\rm stars})$ and $\log_{10}(\rho_{\rm dust}/\rho_{\rm stars})$, with the exception of $\log_{10}(\rho_{\rm gas}/\rho_{\rm stars})$ in the field – the field is much more gas rich than any of the other three environments. However, all four environments are statistically the same with regard to $\log_{10}(\rho_{\rm dust}/\rho_{\rm stars})$. These results again imply that gas is affected by higher density environments much more so than the other significant component of the ISM, dust. We have ordered the mass density ratios in Table 10 from lowest to highest, and they correspond to what we might have expected with the possible exception of the ordering of the filament and Virgo environments.

Given that we have calculated the baryonic mass densities of the Coma cluster (in galaxies), we can also calculate the total mass of each component using our above estimate of its volume (125 Mpc^3). As we have also measured the velocity dispersion of the cluster, we can measure the virial mass of the cluster using

$$M_{\rm virial} = \frac{5 R_{\rm virial} \sigma^2}{G}, \quad (6)$$

where $M_{\rm virial}$, $R_{\rm virial}$, σ and G are the virial mass, virial radius, velocity dispersion and gravitational constant, respectively. In Table 11, we compare the measured baryonic mass of material in galaxies with the total dynamical mass of the cluster. The overall ratio of dynamical mass to baryonic mass (excluding the X-ray gas) of the cluster is ∼104.

8 SUMMARY

We have undertaken a *Herschel* FIR survey of the Coma cluster and the galaxy filament it resides within. Our survey covers an area of

$\sim$150 deg^2 observed in five bands at 100, 160, 250, 350 and 500 μm. We have used the SDSS spectroscopic survey to define an area and redshift selected sample of 744 Coma cluster galaxies – the CCC. For comparison, we also define in a similar way a sample of 951 galaxies in the connecting filament – the CFC.

We have used the optical positions and parameters of these CCC and CFC galaxies to define appropriate apertures to measure their FIR emission. We have detected 99 of 744 (13 per cent) and 422 of 951 (44 per cent) of the cluster and filament galaxies in the SPIRE 250 μm band, which we use for our initial FIR selection. We have carried out simulations to ensure that our process of associating FIR and optical sources leads to less than 5 per cent misidentified objects.

In order to better understand the global detection rates, we have separated the cluster and filament galaxies into three morphological categories using the Galaxy Zoo data: early, $p(\mathrm{E}) > 0.8$; late, $p(\mathrm{S}) > 0.8$ and uncertain where $p(\mathrm{E}) < 0.8$ and $p(\mathrm{S}) < 0.8$. We examined the detection rate for each morphological group in the 250 μm band as it has the highest detection rate of all the *Herschel* bands. Early- and late-type galaxies have the same relative detection rates in the cluster and filament, but overall the fraction of galaxies detected in the cluster is lower because of the morphological mix. The relative detection rates of our 'uncertain' types (S0/Sa?) are noticeably different between the filament (higher rate) and the cluster (lower rate). This is one of the few clear measurements of a difference between the filament and cluster environment.

We compare the cluster velocity dispersions of detected and undetected late-, uncertain- and early-type galaxies. We found that all morphological types have velocity dispersions statically identical to each other and the overall cluster value. This implies that all morphological types have been in the cluster longer than a crossing time and hence longer than the time-scale for ram pressure stripping – the two of which are comparable.

For galaxies detected in all five FIR bands, we fit a modified blackbody with a fixed emissivity index of $\beta = 2$, giving dust masses and temperatures for 198 galaxies. As expected, early-type galaxies show lower dust masses than late-type galaxies, but they tend to have hotter dust temperatures. When comparing the FIR properties of galaxies in Coma and the filament, we find that they are statistically identical with the exception of the hotter temperatures of early-type cluster galaxies.

Combining our data with that from the literature, we estimate the total gas mass as well as the mass in metals (in the gas phase and in the dust) for a sub-sample of Coma and filament galaxies. We find no evidence for a difference in the effective yields of these two populations. This implies that neither population has been subjected to gas loss or infall to a greater or lesser extent than the other population.

We have compared a number of galaxy parameters (dust-to-stars, gas-to-stars, sSFR and morphology) for Coma cluster and filament galaxies and considered how each is affected by local galaxy number density (Σ_1, Σ_5, Σ_{10} and projected cluster radius). Using the Galaxy Zoo weightings of probability of being a spiral (p(S)) or elliptical (p(E)), we defined a new parameter (Φ), where $\Phi = p(\mathrm{S}) - p(\mathrm{E})$. We show that Φ is strongly affected by local number density (environment), which is another way of representing the morphology–density relation (Dressler 1980). We find that the above measured parameters of early-type galaxies appear to be only very weakly or not at all affected by their environment. Late-types also show a weak change in most of the above parameters with environment – the exception being gas-to-stars ratio, which is strongly affected by environmental density on all scales.

In order to understand how the baryonic components of the galaxies change as a whole between the cluster and filament, we have created baryonic mass functions. Using Schechter fits to stellar, gas and dust mass functions for the Coma cluster and filament, we compare their parameters (ϕ, M^* and α) with values found for the Virgo cluster and a field sample. Other than ϕ, which is dependent on a somewhat arbitrary calculation of volume, we found M^* and α to be identical between environments. We calculate the ratio of gas to stellar and dust to stellar mass densities for each environment finding that within the errors Virgo, Fornax, Coma and the filament are all gas deficient when compared to the general field, but that this is not so for the dust. Galaxies in dense environment are far more prone to gas rather than dust loss.

ACKNOWLEDGEMENTS

The H-ATLAS is a project with *Herschel*, which is an ESA space observatory with science instruments provided by European-led Principal Investigator consortia and with important participation from NASA. The H-ATLAS website is http://www.h-atlas.org/.

LD, SM and RI acknowledge support from the ERC in the form of the Advanced Investigator Program, COSMICISM. LD and SM acknowledge support from the European Research Council in the form of Consolidator Grant CosmicDust.

Funding for the Sloan Digital Sky Survey IV has been provided by the Alfred P. Sloan Foundation, the US Department of Energy Office of Science and the Participating Institutions. SDSS-IV acknowledges support and resources from the Center for High-Performance Computing at the University of Utah. The SDSS website is www.sdss.org.

SDSS-IV is managed by the Astrophysical Research Consortium for the Participating Institutions of the SDSS Collaboration including the Brazilian Participation Group, the Carnegie Institution for Science, Carnegie Mellon University, the Chilean Participation Group, the French Participation Group, Harvard-Smithsonian Center for Astrophysics, Instituto de Astrofísica de Canarias, the Johns Hopkins University, Kavli Institute for the Physics and Mathematics of the Universe (IPMU)/University of Tokyo, Lawrence Berkeley National Laboratory, Leibniz Institut für Astrophysik Potsdam (AIP), Max-Planck-Institut für Astronomie (MPIA Heidelberg), Max-Planck-Institut für Astrophysik (MPA Garching), Max-Planck-Institut für Extraterrestrische Physik (MPE), National Astronomical Observatory of China, New Mexico State University, New York University, University of Notre Dame, Observatário Nacional/MCTI, the Ohio State University, Pennsylvania State University, Shanghai Astronomical Observatory, United Kingdom Participation Group, Universidad Nacional Autónoma de México, University of Arizona, University of Colorado Boulder, University of Oxford, University of Portsmouth, University of Utah, University of Virginia, University of Washington, University of Wisconsin, Vanderbilt University and Yale University.

The *Herschel* spacecraft was designed, built, tested and launched under a contract to ESA managed by the *Herschel*/Planck Project team by an industrial consortium under the overall responsibility of the prime contractor Thales Alenia Space (Cannes), and including Astrium (Friedrichshafen) responsible for the payload module and for system testing at spacecraft level, Thales Alenia Space (Turin) responsible for the service module, and Astrium (Toulouse) responsible for the telescope, with in excess of a hundred subcontractors.

This research has made use of the GOLDMINE data base.

EI acknowledges funding from CONICYT/FONDECYT postdoctoral project No.:3130504.

REFERENCES

Asplund M., García Pérez A. E., 2001, A&A, 372, 601
Auld R. et al., 2013, MNRAS, 428, 1880
Bai L., Rieke G. H., Rieke M. J., Hinz J. L., Kelly D. M., Blaylock M., 2006, ApJ, 639, 827
Bell E. F., McIntosh D. H., Katz N., Weinberg M. D., 2003, ApJS, 149, 289
Bianchi S., 2013, A&A, 552, A89
Bicay M. D., Giovanelli R., 1987, ApJ, 321, 645
Binggeli B., Sandage A., Tammann G. A., 1985, AJ, 90, 1681
Boselli A., Gavazzi G., 2006, PASP, 118, 517
Boselli A., Cortese L., Boquien M., Boissier S., Catinella B., Gavazzi G., Lagos C., Saintonge A., 2014, A&A, 564, A67
Brinchmann J., Charlot S., White S. D. M., Tremonti C., Kauffmann G., Heckman T., Brinkmann J., 2004, MNRAS, 351, 1151
Casoli F., Dickey J., Kazes I., Boselli A., Gavazzi P., Baumgardt K., 1996, A&A, 309, 43
Castander F. J. et al., 2001, AJ, 121, 2331
Chapin E. L. et al., 2011, MNRAS, 411, 505
Colless M., Dunn A., 1995, PASP, 12, 122
Colless M., Dunn A. M., 1996, ApJ, 458, 435
Conrow T. P. et al., 1993, BAAS, 25, 1291
Contursi A., Boselli A., Gavazzi G., Bertagna E., Tuffs R., Lequeux J., 2001, A&A, 365, 11
Cortese L., 2012, A&A, 543, A132
Cortese L. et al., 2010, A&A, 518, L49
Cowie L. L., McKee C. F., 1977, ApJ, 211, 135
Cybulski R., Yun M. S., Fazio G. G., Gutermuth R. A., 2014, MNRAS, 439, 3564
Davies J. I. et al., 2010, A&A, 518, L48
Davies J. I. et al., 2011, MNRAS, 415, 1883
Davies J. I. et al., 2012, MNRAS, 419, 3505
Davies J. I. et al., 2014, MNRAS, 438, 1922
Donas J., Milliard B., Laget M., 1995, A&A, 303, 661
Draine B. T., 2003, ARA&A, 41, 241
Draine B. T., Li A., 2007, ApJ, 657, 810
Dressler A., 1980, ApJ, 236, 351
Dunne L. et al., 2011, MNRAS, 417, 1510
Eales S. et al., 2010, PASP, 122, 499
Edmunds M. G., 1990, MNRAS, 246, 678
Edwards L. O. V., Fadda D., 2011, AJ, 142, 148
Ferguson H. C., 1989, AJ, 98, 367
Fuller C. et al., 2014, MNRAS, 440, 1571
Fumagalli M., Krumholz M. R., Prochaska J. X., Gavazzi G., Boselli A., 2009, ApJ, 697, 1811
Gavazzi G., 1989, ApJ, 346, 59
Gavazzi G., Boselli A., 1996, A UBVJHK Photometric Catalogue of 1022 Galaxies in 8 Nearby Clusters. Gordon and Breach, New York
Gavazzi G., Catinella B., Carrasco L., Boselli A., Contursi A., 1998, AJ, 115, 1745
Gavazzi G., Boselli A., Donati A., Franzetti P., Scodeggio M., 2003, A&A, 400, 451
Gavazzi G., O'Neil K., Boselli A., van Driel W., 2006, A&A, 449, 929
Gavazzi G., Fumagalli M., Cucciati O., Boselli A., 2010, A&A, 517, A73
Geller M. J., Diaferio A., Kurtz M. J., 1999, ApJ, 517, L23
Giovanelli R., Haynes M. P., 1985, ApJ, 292, 404
Girardi M., Giuricin G., Mardirossian F., Mezzetti M., Boschin W., 1998, ApJ, 505, 74
Godwin J. G., Peach J. V., 1977, MNRAS, 181, 323
Griffin M. J. et al., 2010, A&A, 518, L3
Gunn J. E., Gott J. R., III, 1972, ApJ, 176, 1
Gupta A., Mathur S., Krongold Y., Nicastro F., Galeazzi M., 2012, ApJ, 756, L8
Haynes M. P. et al., 2011, AJ, 142, 170
Helou G., Walker D. W., eds, 1988, Infrared Astronomical Satellite (IRAS) Catalogs and Atlases. Vol. 7: The Small Scale Structure Catalog. NASA RP-1190
Hickinbottom S. et al., 2014, MNRAS, 442, 1286
Hughes J. P., 1989, ApJ, 337, 21
Ibar E. et al., 2010, MNRAS, 409, 38
Kauffmann G. et al., 2003, MNRAS, 341, 33
Kennicutt R. C., Jr, Bothun G. D., Schommer R. A., 1984, AJ, 89, 1279
Kent S. M., Gunn J. E., 1982, AJ, 87, 945
Kessler M. F. et al., 1996, A&A, 315, L27
Kroupa P., 2002, Science, 295, 82
Kubo J. M., Stebbins A., Annis J., Dell'Antonio I. P., Lin H., Khiabanian H., Frieman J. A., 2007, ApJ, 671, 1466
Lintott C. J. et al., 2008, MNRAS, 389, 1179
Marsden G. et al., 2009, ApJ, 707, 1729
Meyer D. M., Jura M., Cardelli J. A., 1998, ApJ, 493, 222
Mobasher B. et al., 2001, ApJS, 137, 279
Neugebauer G. et al., 1984, ApJ, 278, L1
Panter B., Jimenez R., Heavens A. F., Charlot S., 2007, MNRAS, 378, 1550
Pilbratt G. L. et al., 2010, A&A, 518, L1
Poglitsch A. et al., 2010, A&A, 518, L2
Pohlen M. et al., 2010, A&A, 518, L72
Ramella M., Geller M. J., Huchra J. P., 1992, ApJ, 384, 396
Roediger E., Brüggen M., 2008, MNRAS, 388, L89
Roussel H., 2013, PASP, 125, 1126
Smith M. W. L. et al., 2012, ApJ, 748, 123
Solanes J. M., Manrique A., García-Gómez C., González-Casado G., Giovanelli R., Haynes M. P., 2001, ApJ, 548, 97
Strauss M. A. et al., 2002, AJ, 124, 1810
The L. S., White S. D. M., 1986, AJ, 92, 1248
Tonnesen S., Bryan G. L., van Gorkom J. H., 2007, ApJ, 671, 1434
Tremonti C. A. et al., 2004, ApJ, 613, 898
Verstappen J. et al., 2013, A&A, 556, A54
Werner M. W. et al., 2004, ApJS, 154, 1
Whittet D., 1992, Dust in the Galactic Environment. IoP Publishing, Bristol
Zwicky F., 1951, PASP, 63, 61

SUPPORTING INFORMATION

Additional Supporting Information may be found in the online version of this article:

Appendices.
(http://www.mnras.oxfordjournals.org/lookup/suppl/doi:10.1093/mnras/stw305/-/DC1).

Please note: Oxford University Press is not responsible for the content or functionality of any supporting materials supplied by the authors. Any queries (other than missing material) should be directed to the corresponding author for the paper.

This paper has been typeset from a TEX/LATEX file prepared by the author.